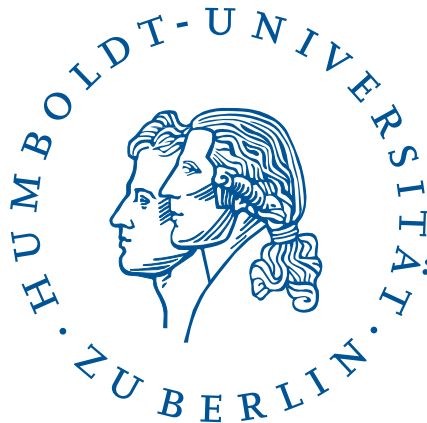


X-Ray Absorption Spectroscopy of Oligothiophene Crystals from *Ab-Initio* Many-Body Theory

MASTERARBEIT

zur Erlangung des akademischen Grades
Master of Science
(M. Sc.)
im Fach Physik



eingereicht an der
Mathematisch-Naturwissenschaftlichen Fakultät
Institut für Physik
Humboldt-Universität zu Berlin

von
Herrn Konstantin Lion
geboren am 25.01.1993 in Berlin

Gutachter:

1. *Prof. Dr. Dr. h. c. Claudia Draxl*
2. *PD Dr. Andreas Opitz*

eingereicht am: 13.10.2017

Acknowledgement

First and foremost, I want to thank my supervisor Claudia Draxl for her guidance and ongoing support during my Master project. I am deeply indebted to her, as she has provided me with many opportunities along the way.

I also want to thank Caterina Cocchi for many fruitful and enlightening discussions. Without her, large portions of this work would not have been possible.

Furthermore, I want to thank Christian Vorwerk and Benjamin Aurich for helping me with any problems occurring during the many calculations. Lastly, I want to express gratitude to the remaining members of Claudia Draxl's research group, for creating a very relaxed and pleasant atmosphere.

Contents

I	Introduction	1
II	Structural Properties of Oligothiophene Crystals	2
III	Theoretical Foundations	4
1	Density-Functional Theory	4
1.1	Hohenberg-Kohn Theorem	4
1.2	Kohn-Sham Formalism	5
1.3	Numerical Solutions of the Kohn-Sham Equations	6
2	Many-Body Perturbation Theory	9
2.1	Dielectric Response	9
2.2	BSE for the Two-Particle Correlation Function	10
2.3	Reformulation of the BSE as an Eigenvalue Problem	11
3	Application to Core Excitations	13
3.1	Effective Hamiltonian	13
3.2	Description of Core States	15
3.3	Description of Conduction States	16
4	X-Ray Absorption Spectroscopy	17
IV	Computational Parameters	19
V	Electronic Structure	20
VI	XANES of Oligothiophene Crystals	23
1	Carbon K Absorption Edge	24
1.1	Analysis of XAS of Crystalline 2T	24
1.2	Dependence on the Oligomer Length	28
2	Sulfur K Absorption Edge	31
2.1	Analysis of XAS of Crystalline 4T	31
2.2	Dependence on the Oligomer length	34
3	Sulfur $L_{2,3}$ Absorption Edge	37
3.1	Analysis of XAS of Crystalline 2T	37
3.2	Dependence on the Oligomer Length	41
VII	Summary and Outlook	46
A	Transformation from Cartesian to Crystalline Axes	54
B	Supplement to Chapter VI	56

I Introduction

With the aim of producing cheap electronics on a large scale, much effort has been devoted to identifying potential active components in electronics and optoelectronics. In this context, organic materials based on π -conjugated molecules emerged as outstanding candidates for organic field effect transistors (OFETs) [1], organic solar cells (OSCs) [2], and organic light emitting diodes (OLEDs) [3, 4] due to their visible light-matter interaction and low molecular weight. Among them, oligo- and poly-thiophenes offer the unique combination of chemical stability, efficient electronic conjugation, and synthetic flexibility which allows for the deliberate adjustment of properties through substitution at the thiophene ring [5]. Poly (3-hexylthiophene) (P3HT) has already established itself as an organic semiconductor for OFETs and OSCs [6, 7]. Oligothiophenes bear the advantage of having a well defined structure, and thus producing more defect-free thin films compared to polythiophenes. Among others, α -sexithiophene proves to be a very promising candidate for the use in OFETs [8].

To optimize the performance of these materials, extensive knowledge of their chemical composition and fundamental properties, including electronic structure and their response to electro-magnetic radiation, is required. X-ray absorption spectroscopy (XAS) represents a powerful technique for this purpose. It is used to determine the local geometric and electronic structure of a material, and can identify the chemical fingerprint of elements and detect specific bonds in molecules [9]. First-principles calculations are invaluable in interpreting such experimental data. Density-functional theory (DFT), mainly in the core-hole approximation [10], is often applied to simulate XAS in organic materials. While this approach is fairly accurate for K absorption edges, it falls short to reproduce other absorption edges where coupling effects between the subedges are important. Here, a fully relativistic approach with an explicit treatment of the electron-hole interaction is a significant step forward [11–13]. Many-body perturbation theory (MBPT) represents the state-of-the-art formalism to calculate neutral excitations in solids [12]. In this work, we calculate XAS from *ab-initio* MBPT by treating the electron-hole interaction through the solution of the Bethe-Salpeter equation (BSE), using a fully relativistic treatment of the core states [11, 14]. By using a (L)APW+lo basis set, we treat all electrons on the same footing, which allows for accessing the core region. This approach is implemented within the all-electron full potential **exciting** code for DFT and MBPT calculations [15]. It was previously successfully applied to a number of absorption edges [12], such as the nitrogen K edge of azobenzene monolayers [16] and the titanium $L_{2,3}$ absorption edge of TiO_2 [14].

Core excitations in oligothiophenes ($n\text{T}$, n is number of monomer rings) were previously explored mainly for short oligomers such as 2T [17–22]. A thorough investigation of XAS and the electronic structure for longer oligomers is still missing. In this work, we study the carbon K , sulfur K , and sulfur $L_{2,3}$ absorption edges in crystalline 2T , 4T , and 6T . When available, our results are compared with published experimental data. By considering transitions from core states of inequivalent atoms, we probe their individual chemical environment. We discuss the properties of core excitations, i.e., exciton binding energies and spectral features, in relation with the oligomer length and analyze their excitonic character.

II Structural Properties of Oligothiophene Crystals

In this work, we investigate crystals of oligothiophenes (nT) with an even number of rings: bithiophene (2T), quaterthiophene (4T), and sexithiophene (6T). In Fig. 2.1, we illustrate the oligothiophene monomer with n representing the number of rings in the oligomer. Each thiophene ring consists of sp^2 hybridized carbon (C) and sulfur (S) atoms, as well as hydrogen (H) atoms. S atoms form two covalent σ bonds while C atoms form three covalent σ bonds. The remaining six valence electrons, one from each C atom and two from the S atom, remain in $2p$ orbitals perpendicular to the molecular plane, thus forming the aromatic π -electron cloud. The aromatic character leads to the (quasi) planar form of the oligothiophene molecules which is preserved in the crystalline phase [5, 23].

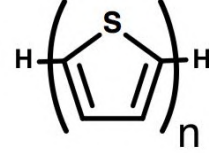


Figure 2.1: The oligothiophene molecule α - nT . The number of repeating thiophene rings is indicated by n .

The lattice parameters of oligothiophenes at ambient conditions and the chemical formulas of all investigated materials are given in Tab. II.1. In this work, we perform calculations for α - nT ¹ where the thiophene rings are connected at the α -C site, i.e., the C atoms with covalent bonds to the S atoms. The structure of oligothiophene crystals is characterized by the *herringbone* arrangement of multiple inequivalent molecules in the unit cell. These molecules interact with each other through van der Waals forces. Such an arrangement is commonly found in organic crystals consisting of planar linear molecular chains [24]. In the case of α -2T, two inequivalent molecules are in each unit cell [25]. Dependent on the growth conditions, two different polymorphs have been identified for α -4T [26, 27] and α -6T [28, 29]: a high temperature phase (HT) and a low temperature phase (LT) with two and four inequivalent molecules per unit cell, respectively. In this work, we solely focus on the HT polymorphs with two molecules in the unit cell to directly compare our results between the different oligothiophenes. All investigated materials crystallize in a monoclinic structure: α -2T belongs to the $P2_1/c$ space group, whereas α -4T/HT and α -6T/HT to the $P2_1/a$ space group. The unit cells of the 2T, 4T, and 6T crystals is shown in Fig. 2.2. The long molecular axis is approximately aligned with the **c** axis. This is reflected in the increase of the lattice parameter c with increasing oligomer length n . The other lattice parameters, b and a , are comparable in value for all investigated systems. Here, the short molecular axis is approximately aligned with the **b** axis. This anisotropy of the molecule leads to the highly anisotropic electronic and optical properties observed in oligothiophenes [5, 23].

¹ α - nT is also referred to as 2,2'- nT .

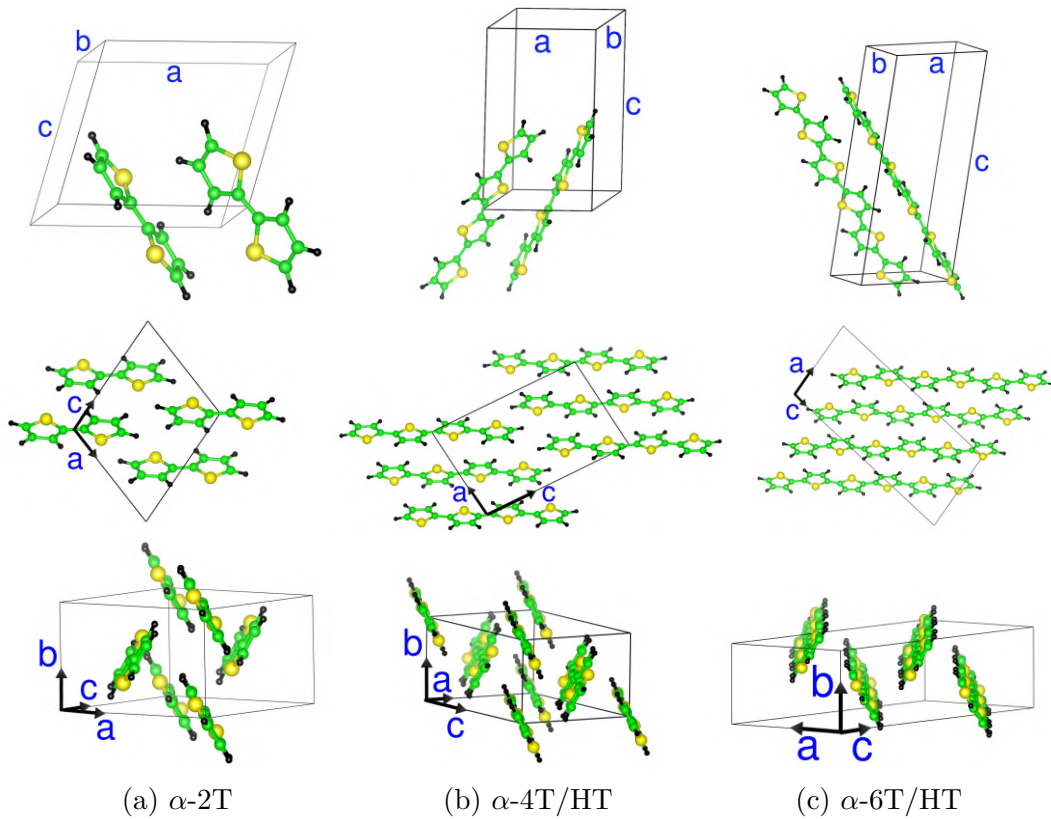


Figure 2.2: Unit cell (top), the ac plane (middle), and the herringbone arrangement of two inequivalent molecules (bottom) for 2T, 4T, and 6T crystals. C atoms are in green, S atoms in yellow, and H atoms in black.

Table II.1: Lattice parameters of oligothiophene crystals from [25, 26, 30].

	$a[\text{\AA}]$	$b[\text{\AA}]$	$c[\text{\AA}]$	$\beta[^\circ]$
α -2T $\text{C}_8\text{H}_8\text{S}_2$	8.81	5.77	7.87	107.1
α -4T/HT $\text{C}_{16}\text{H}_{16}\text{S}_4$	8.93	5.75	14.34	97.2
α -6T/HT $\text{C}_{24}\text{H}_{24}\text{S}_6$	9.14	5.68	20.67	97.8

III Theoretical Foundations

This chapter introduces the theoretical concepts needed to calculate XAS from *ab-initio* many-body perturbation theory. Section 1 introduces density functional theory, focusing on the Kohn-Sham formalism and the expansion of the resulting equations in the (L)APW+lo basis set. In Section 2, we describe the main concepts of many-body perturbation theory which are most relevant for this work. Section 3 presents its application to core excitations, while Section 4 introduces the basics of X-ray absorption spectroscopy.

1 Density-Functional Theory

All properties of a system of interacting particles, such as electrons and nuclei, can be obtained by solving the many-body Schrödinger equation. However, for realistic systems, this task is impossible to solve due to the high amount of degrees of freedom. It is therefore necessary to introduce approximations for any practical applications. The Born-Oppenheimer approximation [31] serves as a first simplification: The nuclei can be viewed as almost stationary compared to the electrons, enabling the separation of the electronic and nuclear wavefunctions. One now has to solve the equation for the electronic wavefunction $\Psi(\mathbf{r}_1, \dots, \mathbf{r}_N)$ ¹

$$E \Psi(\mathbf{r}_1, \dots, \mathbf{r}_N) = [\hat{T} + \hat{U} + \hat{V}] \Psi(\mathbf{r}_1, \dots, \mathbf{r}_N) \quad (1.1)$$

$$= \left[-\sum_i \frac{\nabla_i^2}{2} + \frac{1}{2} \sum_{i \neq j} \frac{1}{|\mathbf{r}_i - \mathbf{r}_j|} - \sum_{i,I} \frac{Z_I}{|\mathbf{r}_i - \mathbf{R}_I|} \right] \Psi(\mathbf{r}_1, \dots, \mathbf{r}_N), \quad (1.2)$$

where N represents the number of interacting electrons in a potential of nuclei with atomic number Z_I at position \mathbf{R}_I .

The exact electronic wavefunction, determined by $3N$ independent variables, can be obtained as a linear combination of Slater determinants. This approach is known as the configuration interaction method. While this method can be applied to small systems, its computational cost for extended systems is scaling unfavorably.

Density-functional theory (DFT) serves as an alternative approach, as it enables to calculate the electron density $n(\mathbf{r})$ instead of the electronic wavefunction. The main advantage of this approach is that the number of independent variables is reduced to the 3 spatial coordinates, thereby ensuring excellent scalability to larger systems. All observables can be expressed as functionals of the electron density. The Hohenberg-Kohn theorem is the foundation of DFT.

1.1 Hohenberg-Kohn Theorem

The basic lemma of Hohenberg and Kohn states that the external potential $v_{\text{ext}}(\mathbf{r})$ is a unique functional of the ground-state density $n(\mathbf{r})$ of an inhomogeneous interacting electron gas [32]. The full electronic Hamiltonian \hat{H} is therefore defined by the

¹Note that atomic units are used in this thesis.

electron density and one can express the total energy of the system as

$$E_v[n(\mathbf{r})] = F[n(\mathbf{r})] + \int v_{\text{ext}}(\mathbf{r}) n(\mathbf{r}) d^3r, \quad (1.3)$$

where the universal functional $F[n(\mathbf{r})]$ is independent of the external potential and contains the kinetic energy and interaction potential between the electrons. The ground-state energy E can be obtained from the Rayleigh-Ritz variational principle:

$$E = \min_{\tilde{\Psi}} \langle \tilde{\Psi} | \hat{H} | \tilde{\Psi} \rangle, \quad (1.4)$$

where $\tilde{\Psi}$ represents a normalized trial wavefunction for the electron system. The Hohenberg-Kohn theorem states that this variational principle can equivalently be formulated in terms of trial densities $\tilde{n}(\mathbf{r})$:

$$E = \min_{\tilde{n}(\mathbf{r})} E_v[\tilde{n}(\mathbf{r})] \quad (1.5)$$

$$= \min_{\tilde{n}(\mathbf{r})} \left\{ F[\tilde{n}(\mathbf{r})] + \int v_{\text{ext}}(\mathbf{r}) \tilde{n}(\mathbf{r}) d^3r \right\}. \quad (1.6)$$

1.2 Kohn-Sham Formalism

The Hohenberg-Kohn theorem ensures that the ground state energy is determined by the minimization with respect to trial densities. What is missing, however, is an expression for the functional $F[n(\mathbf{r})]$. Kohn and Sham [33] proposed the following:

$$F[n(\mathbf{r})] = T_0[n(\mathbf{r})] + \frac{1}{2} \int \int \frac{n(\mathbf{r})n(\mathbf{r}')}{|\mathbf{r} - \mathbf{r}'|} d^3r d^3r' + E_{\text{XC}}[n(\mathbf{r})] \quad (1.7)$$

$$= T_0[n(\mathbf{r})] + E_{\text{H}}[n(\mathbf{r})] + E_{\text{XC}}[n(\mathbf{r})], \quad (1.8)$$

where the first term represents the kinetic energy of non-interacting electrons, the second term the Hartree energy, and the third term the exchange-correlation functional. The minimization in Eq. (1.6) using a Lagrange multiplier ϵ under the constraint of constant electron number N , leads to:

$$\delta E[\tilde{n}(\mathbf{r})] = \int \left(\frac{\delta T_0[n(\mathbf{r})]}{\delta \tilde{n}(\mathbf{r})} + \frac{1}{2} \int \frac{\tilde{n}(\mathbf{r}')}{|\mathbf{r} - \mathbf{r}'|} d^3r' + \frac{\delta E_{\text{XC}}[n(\mathbf{r})]}{\delta \tilde{n}(\mathbf{r})} - \epsilon \right) \Big|_{\tilde{n}(\mathbf{r})=n(\mathbf{r})} \delta \tilde{n}(\mathbf{r}) d^3r. \quad (1.9)$$

This equation resembles the problem of non-interacting electrons in an effective potential v_{KS} :

$$v_{\text{KS}} = \frac{\delta E_{\text{H}}(\mathbf{r}, [n])}{\delta n(\mathbf{r})} + \frac{\delta E_{\text{XC}}(\mathbf{r}, [n])}{\delta n(\mathbf{r})} + v_{\text{ext}}(\mathbf{r}), \quad (1.10)$$

where the first term represents the mean-field interaction of the electrons, the second term the exchange-correlation potential, and the third term the external Coulomb potential due to the nuclei. The ground state density can now be obtained by solving the set of one-particle Schrödinger equations

$$\left(-\frac{\nabla^2}{2} + v_{\text{KS}}(\mathbf{r}; [n]) \right) \varphi_{\gamma}(\mathbf{r}) = \varepsilon_{\gamma} \varphi_{\gamma}(\mathbf{r}), \quad (1.11)$$

where the density is calculated as

$$n(\mathbf{r}) = \sum_{\gamma=1}^N |\varphi_{\gamma}(\mathbf{r})|^2. \quad (1.12)$$

These equations are known as the Kohn-Sham equations and have to be solved self-consistently according to the scheme illustrated in Fig. (3.1). This will result in the exact ground state energy and density if no approximations are made. It is important to note that the Kohn-Sham wavefunctions and eigenvalues do not represent the single-particle wavefunctions and eigenvalues of the many-body system.

A problem arises for practical applications when examining the exchange-correlation functional. Its exact form is to this day unknown. As a result, the accuracy of the DFT calculation depends on the level of approximation for E_{XC} . Many approximations for the exchange-correlation functional with varying accuracy have been proposed in the literature. The local-density approximation (LDA) [34] is often employed due to its low computational cost. In this framework the exchange-correlation functional takes on the form:

$$E_{XC}^{LDA}(n(\mathbf{r})) = \int e_{xc}(n(\mathbf{r})) n(\mathbf{r}) d\mathbf{r}^3, \quad (1.13)$$

where $e_{xc}(n(\mathbf{r}))$ is the exchange-correlation energy per particle of the uniform electron gas. Another type of functional is given by the generalized gradient approximation (GGA) which includes the gradient of the electron density. This partially accounts for the non-locality of the exchange-correlation functional. One popular GGA functional was developed by Perdew, Burke, and Ernzerhof (PBE) [35]. It includes the gradient correction without introducing any additional experimental parameters, thereby ensuring its applicability to a wide range of systems. These functionals, however, can not accurately describe electron dispersion, i.e. van der Waals interaction. As a result, they are inaccurate in describing molecular crystals [36]. As reviewed by Klimeš and Michaelides [37], several corrections have been proposed in recent years. For an overview of the different approaches we refer to references [36–38]. In this work, we employ the LDA functional and as such, we expect our obtained results to slightly differ from experimental results.

1.3 Numerical Solutions of the Kohn-Sham Equations

The differential Kohn-Sham equation (1.11) has to be solved numerically. The Kohn-Sham wavefunctions are thus expanded in a basis set $\phi_\gamma(\mathbf{r})$

$$\psi_\gamma(\mathbf{r}) = \sum_{p=1}^P c_\gamma^p \phi_\gamma^p(\mathbf{r}), \quad (1.14)$$

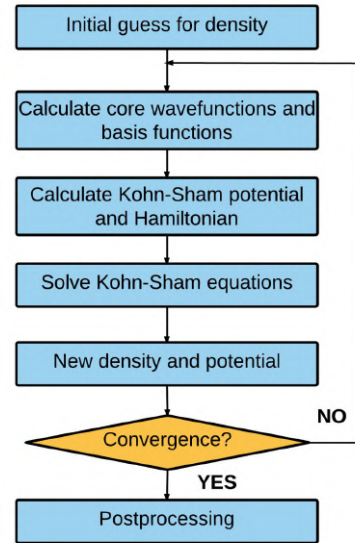


Figure 3.1: Flowchart for the self-consistent solution of the Kohn-Sham equations using an unspecified basis set.

that properly describes physical properties. Inserting Eq. (1.14) into Eq. (1.11), yields the eigenvalue problem:

$$(H - \varepsilon_\gamma O)\mathcal{C} = 0. \quad (1.15)$$

Here, the Hamiltonian H is defined as

$$H_{il} = \left\langle \phi_\gamma^i \left| -\frac{\nabla^2}{2} + v_{\text{KS}} \right| \phi_\gamma^l \right\rangle, \quad (1.16)$$

and O represents the overlap matrix with the elements

$$O_{il} = \left\langle \phi_\gamma^i \left| \phi_\gamma^l \right\rangle. \quad (1.17)$$

The eigenvector \mathcal{C} contains the coefficients c_γ given in Eq. (1.14). The eigenvalues are then obtained by diagonalizing the matrix in Eq. (1.15). In order to keep computational cost manageable, only a limited amount of basis functions P can be taken into account. It is therefore essential to choose a basis set that requires only few basis functions while providing sufficient accuracy.

The (L)APW-lo basis set [39] is employed for all the calculations in this work and will be introduced briefly. Electrons far away from the nuclei act as almost free electrons and can accurately be described by planewaves. Electronic wavefunctions near the nuclei resemble atomic-like wavefunctions. As a result, one can separate the space into two regions, the interstitial (I) region and the muffin-tin (MT) spheres. The latter are non-overlapping spheres with radius R_{MT} centered on the atoms labeled by \mathbf{R}_α .² The interstitial region fills the remaining space between the muffin-tins. In the augmented planewave (APW) basis set, the Kohn-Sham wavefunctions can then be expressed as [40]

$$\psi_{nk}(\mathbf{r}) = \sum_{\mathbf{G}} c_{n\mathbf{G}}^k \phi_{\mathbf{k}+\mathbf{G}}(\mathbf{r}), \quad (1.18)$$

with

$$\phi_{\mathbf{k}+\mathbf{G}}(\mathbf{r}) = \begin{cases} \sum_{lm} A_{lm\alpha}^{\mathbf{k}+\mathbf{G}} u_{l\alpha}(r_\alpha, \varepsilon_{nk}) Y_{lm}(\hat{\mathbf{r}}_\alpha), & r_\alpha \leq R_{\text{MT}} \\ \frac{1}{\sqrt{\Omega}} e^{i(\mathbf{k}+\mathbf{G})\cdot\mathbf{r}}, & \mathbf{r} \in I \end{cases}, \quad (1.19)$$

where $\mathbf{r}_\alpha = \mathbf{r} - \mathbf{R}_\alpha$ and Ω represents the unit cell volume. Here, the MT sphere is expanded in terms of spherical harmonics $Y_{lm}(\hat{\mathbf{r}}_\alpha)$ and radial functions $u_{l\alpha}(r_\alpha, \varepsilon_{nk})$. The coefficients $A_{lm\alpha}^{\mathbf{k}+\mathbf{G}}$ are defined by the continuity condition at the sphere boundary. In order to linearize the eigenvalue problem, the radial function $u_{l\alpha}(r_\alpha, \varepsilon_{nk})$ is expanded to first order around the linearization energy:

$$u_{l\alpha}(r_\alpha, \varepsilon_{nk}) \approx u_{l\alpha}(r_\alpha, \varepsilon_{l\alpha}) + (\varepsilon_{l\alpha} - \varepsilon_{nk}) \underbrace{\left. \frac{\partial u_{l\alpha}(r_\alpha, \varepsilon)}{\partial \varepsilon} \right|_{\varepsilon=\varepsilon_{l\alpha}}}_{\dot{u}_{l\alpha}(r_\alpha, \varepsilon_{l\alpha})}. \quad (1.20)$$

²Note that muffin-tin radii can differ for different atomic species.

This defines the linearized augmented planewave (LAPW) basis set [39]:

$$\phi_{\mathbf{k}+\mathbf{G}}(\mathbf{r}) = \begin{cases} \sum_{lm} \left[A_{lm\alpha}^{\mathbf{k}+\mathbf{G}} u_{l\alpha}(r_\alpha, \varepsilon_{l\alpha}) + B_{lm\alpha}^{\mathbf{k}+\mathbf{G}} \dot{u}_{l\alpha}(r_\alpha, \varepsilon_{l\alpha}) \right] Y_{lm}(\hat{\mathbf{r}}_\alpha), & r_\alpha \leq R_{\text{MT}} \\ \frac{1}{\sqrt{\Omega}} e^{i(\mathbf{k}+\mathbf{G})\cdot\mathbf{r}}, & \mathbf{r} \in I \end{cases}. \quad (1.21)$$

The coefficient $B_{lm\alpha}^{\mathbf{k}+\mathbf{G}}$ is introduced due to the unknown quantity $(\varepsilon_{l\alpha} - \varepsilon_{nk})$. The continuity condition of $\phi_{\mathbf{k}+\mathbf{G}}(\mathbf{r})$ as well as its spatial derivative at the muffin-tin boundary determine the coefficients $A_{lm\alpha}^{\mathbf{k}+\mathbf{G}}$ and $B_{lm\alpha}^{\mathbf{k}+\mathbf{G}}$. Such an approach, however, harbors additional problems such as the disability to describe states with the same l but different principal quantum numbers. This applies to cases where the elements have valence as well as core electrons.

Alternatively, one can introduce local orbitals (lo) [41], that are only defined within the MT spheres

$$\phi_\beta(\mathbf{r}) = \begin{cases} \delta_{\alpha\alpha\beta} \delta_{l\beta} \delta_{mm\beta} [a_\beta u_{l\alpha}(r_\alpha, \varepsilon_{l\alpha}) + b_\beta \dot{u}_{l\alpha}(r_\alpha, \varepsilon_{l\alpha})] Y_{lm}(\hat{\mathbf{r}}_\alpha), & r_\alpha \leq R_{\text{MT}} \\ 0, & \mathbf{r} \in I \end{cases}, \quad (1.22)$$

and are added to the (L)APW basis functions with fixed energy parameters. Here, the parameters a_α and b_β are determined by the continuity condition of $\phi_\beta(\mathbf{r})$ and its normalization to one. With this the (L)APW+lo basis set is defined as:

$$\psi_{nk}(\mathbf{r}) = \sum_{\mathbf{G}} c_{n\mathbf{G}}^{\mathbf{k}} \phi_{\mathbf{k}+\mathbf{G}}(\mathbf{r}) + \sum_{\beta} c_{n\beta}^{\mathbf{k}} \phi_\beta(\mathbf{r}). \quad (1.23)$$

Compared to the LAPW basis set, this introduction of local orbitals results in a smaller linearization error while the error in the total energy is still $\mathcal{O}(\varepsilon_{l\alpha} - \varepsilon_{nk})^4$ [15].

The basis is now completely defined and can be used to solve Eq. (1.15). The dimension of the matrices H and O are limited by the condition $|\mathbf{k} + \mathbf{G}| \leq G_{\text{max}}$. This planewave cutoff G_{max} alone is not an appropriate parameter: If the muffin-tin radius R_{MT} is reduced, more planewaves are required to accurately describe the interstitial region where the wavefunction is now varying more strongly. In other words, a decrease of R_{MT} requires an increase of G_{max} in order to achieve the same level of accuracy. Therefore, a more appropriate dimensionless cutoff parameter is the product $R_{\text{MT}}^{\text{min}} G_{\text{max}}$, where $R_{\text{MT}}^{\text{min}}$ corresponds to the smallest MT radius in the considered system.

2 Many-Body Perturbation Theory

Density functional theory allows for the calculation of the ground state properties of a system. It fails, however, in describing its excited states.

Absorption spectroscopy probes neutral excitations: An electron is excited to an unoccupied state, by absorbing an incoming photon, while leaving behind an unoccupied state, a *hole*. The electron and the hole interact with each other and also with the remaining electrons in the system. As a result, one is confronted with a complicated many-body problem. Many-body perturbation theory (MBPT) is able to simplify this problem by mapping the many-body problem to a set of single-particle problems. To achieve this, electron and hole are treated as quasiparticles, i.e. effective states dressed by the full interaction with the many-body system. They interact with each other through the Coulomb interaction that is screened by the remaining electrons. To describe quasi-holes and quasi-electrons simultaneously, an effective two-particle Hamiltonian is introduced. It is derived from a two-particle Green's function formalism.

This section provides the main concepts of MBPT that are relevant to the theoretical treatment of X-ray absorption spectroscopy. A more detailed treatment of MBPT and its application to neutral excitations can be found in [42–46].

2.1 Dielectric Response

The electric displacement \mathbf{D} is linearly related to the electric field \mathbf{E} by the microscopic dielectric tensor ϵ :³

$$D_i(\mathbf{r}, \omega) = \int \epsilon_{ij}(\mathbf{r}, \mathbf{r}', \omega) E_j(\mathbf{r}, \omega) d^3r'. \quad (2.24)$$

The dielectric tensor describes the linear response of a system to an external electromagnetic field. It can also be expressed in terms of the complete polarization P :

$$\epsilon^{-1}(\mathbf{r}, \mathbf{r}', \omega) = \delta(\mathbf{r}, \mathbf{r}') + \int v(\mathbf{r}, \mathbf{r}'') P(\mathbf{r}', \mathbf{r}'', \omega) d^3r'', \quad (2.25)$$

where $v(\mathbf{r}, \mathbf{r}'')$ represents the bare Coulomb potential. In a crystal with translational symmetry, the dielectric tensor can be Fourier-transformed into reciprocal space:

$$\epsilon(\mathbf{r}, \mathbf{r}', \omega) = \frac{1}{\Omega} \sum_{\mathbf{q}} \sum_{\mathbf{G}, \mathbf{G}'} e^{-i(\mathbf{q}+\mathbf{G})\mathbf{r}} \epsilon(\mathbf{q} + \mathbf{G}, \mathbf{q} + \mathbf{G}', \omega) e^{-i(\mathbf{q}+\mathbf{G}')\mathbf{r}'}. \quad (2.26)$$

Here, \mathbf{q} is a vector from the first Brillouin zone, \mathbf{G} and \mathbf{G}' are reciprocal lattice vectors, and Ω is the crystal volume. When discussing about optical spectroscopy, one is typically interested in the average response of the system rather than in the response on the atomic scale. The average response is given by the macroscopic dielectric function $\epsilon_M(\mathbf{q}, \omega)$. It is defined by the $\mathbf{G} = \mathbf{G}' = 0$ component of the inverse microscopic dielectric tensor:

$$\epsilon_M(\mathbf{q}, \omega) = \frac{1}{\epsilon^{-1}(\mathbf{q}, \mathbf{q}, \omega)}. \quad (2.27)$$

³This is only valid for linear homogeneous materials.

According to Eq. (2.25), the inverse microscopic dielectric function can be obtained by calculating the complete polarization P . Matrix inversion then yields the macroscopic dielectric function, see Eq. (2.27).

2.2 BSE for the Two-Particle Correlation Function

The calculation of the complete polarization P is performed by solving the Bethe-Salpeter equation (BSE) for the two-particle correlation function L [44]:

$$P(1, 2) = -iL(1, 1, 2, 2), \quad (2.28)$$

where

$$L(1, 1', 2, 2') = G_2(1, 1', 2, 2') - G(1', 2')G(1, 2). \quad (2.29)$$

$G_2(1, 1', 2, 2')$ represents the two-particle Green's function and the $G(1', 2')$, $G(1, 2)$ single-particle Green's functions. The two-particle correlation function L is then defined as the two-particle Green's function G_2 excluding the disconnected part, represented as the product of single-particle Green's functions G . Note that we have introduced the notation of $(1) \rightarrow (\mathbf{r}_1, t_1)$.

The Bethe-Salpeter equation for $L(1, 1', 2, 2')$ assumes the form of a Dyson's-like equation:

$$L(1, 1', 2, 2') = L_0(1, 1', 2, 2') + \int d(3, 3', 4, 4') L_0(1, 1', 3, 3') \Xi(3, 3', 4, 4') L(4, 4', 2, 2'), \quad (2.30)$$

where the function L_0 is introduced as the independent motion of two particles

$$L_0(1, 1', 2, 2') = G(1', 2')G(2, 1), \quad (2.31)$$

and the kernel Ξ contains the effective two-particle interaction. It is obtained as the functional derivative of the Hartree potential V_H and self-energy Σ with respect to the single-particle Green's function:

$$\Xi(3, 3', 4, 4') = \frac{\partial [V_H(4, 4') + \Sigma(4, 4')]}{\partial G(3, 3')}. \quad (2.32)$$

The Hartree potential V_H can also be defined in terms of single-particle Green's functions as⁴:

$$V_H(4, 4') = -i\delta(4, 4') \int G(5, 5^+) v(5, 4) d(5). \quad (2.33)$$

The challenge now is to calculate the interaction kernel Ξ in a numerically manageable way. For this purpose, approximations for the self energy Σ are needed, such as setting the self-energy in Eq. (2.32) to zero. In this approach (Hartree approximation), the particles in the system behave as free particles in a self-consistent

⁴We introduce the notation $1^+ \rightarrow (\mathbf{r}_1, t_1 + 0^+)$.

potential field.

A more sophisticated approximation to the interaction kernel Ξ is to replace the self energy in Eq. (2.32) by the self energy in the *GW*-approximation [47].

In this approach, the self energy Σ is given as [46, 47]:

$$\Sigma(1, 2) = iG(1, 2)W(1, 2). \quad (2.34)$$

Here, W is the dynamically-screened Coulomb interaction

$$W(1, 2) = \int \epsilon^{-1}(1, 3)v(3, 2)d(3), \quad (2.35)$$

with the dielectric matrix expressed in the random phase approximation (RPA):

$$\epsilon(1, 2) = \delta(1, 2) + i \int v(1, 3)G(2, 3)G(3, 2)d(3). \quad (2.36)$$

The interaction kernel Ξ can be obtained by inserting Eqs. (2.33) and (2.34) into Eq. (2.32):

$$\Xi(3, 3', 4, 4') = -i\delta(3, 3')\delta(4, 4')v(3, 4) + i\delta(3, 4)\delta(3', 4')W(3, 3') + iG(4, 4')\frac{\partial W(4, 4')}{\partial G(3, 3')}. \quad (2.37)$$

The first term represents the unscreened exchange interaction, while the second one contains the electron-hole attraction given by the screened interaction W . The third term is commonly neglected in the numerical evaluation of the BSE as it is much smaller compared to the two other terms [48]. As a result, the interaction kernel takes on the form:

$$\Xi(3, 3', 4, 4') = -i\delta(3, 3')\delta(4, 4')v(3, 4) + i\delta(3, 4)\delta(3', 4')W(3, 3'). \quad (2.38)$$

2.3 Reformulation of the BSE as an Eigenvalue Problem

The numerical calculation of the Bethe-Salpeter equation (2.30) requires a reformulation from an integral equation to a matrix eigenvalue problem. The main concepts are introduced in the following. A detailed derivation can be found in [44, 45].

In a crystal, the four-point functions L , L_0 and Ξ must all obey the translational symmetry, i.e. for a given lattice vector \mathbf{R} :

$$L(\mathbf{r}_1 + \mathbf{R}, \mathbf{r}'_1 + \mathbf{R}, \mathbf{r}_2 + \mathbf{R}, \mathbf{r}'_2 + \mathbf{R}) = L(\mathbf{r}_1, \mathbf{r}'_1, \mathbf{r}_2, \mathbf{r}'_2). \quad (2.39)$$

Thus, we can express the four-point functions as a sum of $L_{\mathbf{q}}$, where \mathbf{q} is a vector from the first Brillouin zone and $L_{\mathbf{q}}$ inhibits the full symmetry of the crystal:

$$L(\mathbf{r}_1, \mathbf{r}'_1, \mathbf{r}_2, \mathbf{r}'_2) = \sum_{\mathbf{q}} L_{\mathbf{q}}(\mathbf{r}_1, \mathbf{r}'_1, \mathbf{r}_2, \mathbf{r}'_2). \quad (2.40)$$

The vector \mathbf{q} can be identified as the momentum transfer of the transitions. In this work, we consider the optical limit of X-ray spectroscopy, $\mathbf{q} \rightarrow 0$, and thus

we only consider the L_0 contribution. It will be denoted as $L(\mathbf{r}_1, \mathbf{r}'_1, \mathbf{r}_2, \mathbf{r}'_2)$. This function can be expanded in terms of a complete set of Bloch functions which will be approximated by the Kohn-Sham wavefunctions⁵:

$$L(\mathbf{r}_1, \mathbf{r}'_1, \mathbf{r}_2, \mathbf{r}'_2) = \sum_{i_1, i_2, i_3, i_4} \psi_{i_1}^*(\mathbf{r}_1) \psi_{i_2}(\mathbf{r}'_1) \psi_{i_3}(\mathbf{r}_2) \psi_{i_4}^*(\mathbf{r}'_2) L_{(i_1 i_2), (i_3 i_4)}. \quad (2.41)$$

With this, the correlation function can be expressed as the matrix equation:

$$L_{(i_1 i_2), (i_3 i_4)}(\omega) = \sum_{j_3 j_4} \left[1 - L^0(\omega) \Xi \right]_{(i_1 i_2), (j_3 j_4)}^{-1} L_{(j_3 j_4), (i_3 i_4)}^0. \quad (2.42)$$

Using the representation of the Green's function in the GW -approximation, the function L^0 can be expressed as

$$L_{(i_1 i_2), (i_3 i_4)}^0 = -i \frac{(f_{i_2} - f_{i_1}) \delta_{i_1 i_3} \delta_{i_2 i_4}}{\epsilon_{i_2} - \epsilon_{i_1} - \omega - i\delta}, \quad (2.43)$$

where ϵ represents the single-particle energies and f the Fermi-Dirac distribution function. We introduce an excitonic Hamiltonian H^e defined as

$$H_{(i_1 i_2), (i_3 i_4)}^e = (\epsilon_{i_2} - \epsilon_{i_1}) \delta_{i_1 i_3} \delta_{i_2 i_4} - i(f_{i_2} - f_{i_1}) \Xi_{(i_1 i_2), (i_3 i_4)}, \quad (2.44)$$

and obtain:

$$L_{(i_1 i_2), (i_3 i_4)}(\omega) = i [H^e - \omega]_{(i_1 i_2), (i_3 i_4)}^{-1} (f_{i_4} - f_{i_3}). \quad (2.45)$$

⁵The notation $i_1 = n_1 \mathbf{k}_1$, $(i_1 i_2) = (n_1 \mathbf{k}_1, n_2 \mathbf{k}_2 - \mathbf{q})$ with the quantum numbers $n\mathbf{k}$ is introduced.

3 Application to Core Excitations

In this section we introduce the concepts of MBPT for calculating the macroscopic dielectric tensor that are needed for X-ray absorption spectroscopy. The implementation of optical and X-ray absorption spectroscopy within the (L)APW+lo formalism is discussed in [15, 44] and [14], respectively.

3.1 Effective Hamiltonian

The BSE for the two-particle correlation function L is reformulated as a matrix eigenvalue problem in section (2.3). In the case of core spectroscopy, one can simplify Eq. (2.45): All transitions occur from fully occupied core states c ($f_c = 1$) to fully unoccupied conduction states u ($f_u = 0$). The Dirac-Fermi distribution functions f can be inserted into Eq. (2.45) and yield a reduced excitonic Hamiltonian⁶

$$H_e = \begin{pmatrix} H_{c_1 u_1 \mathbf{k}_1, c_2 u_2 \mathbf{k}_2}^e & H_{c_1 u_1 \mathbf{k}_1, u_2 c_2 \mathbf{k}_2}^e \\ H_{u_1 c_1 \mathbf{k}_1, c_2 u_2 \mathbf{k}_2}^e & H_{u_1 c_1 \mathbf{k}_1, u_2 c_2 \mathbf{k}_2}^e \end{pmatrix}, \quad (3.46)$$

where the block matrices can be written as:

$$H_{c_1 u_1 \mathbf{k}_1, c_2 u_2 \mathbf{k}_2}^e = (\epsilon_{u_1 \mathbf{k}_1} - \epsilon_{c_1}) \delta_{c_1 c_2} \delta_{u_1 u_2} + i \Xi_{c_1 u_1 \mathbf{k}_1, c_2 u_2 \mathbf{k}_2} \quad (3.47)$$

$$H_{c_1 u_1 \mathbf{k}_1, u_2 c_2 \mathbf{k}_2}^e = i \Xi_{c_1 u_1 \mathbf{k}_1, u_2 c_2 \mathbf{k}_2} \quad (3.48)$$

$$H_{u_1 c_1 \mathbf{k}_1, c_2 u_2 \mathbf{k}_2}^e = - \left[H_{c_1 u_1 \mathbf{k}_1, u_2 c_2 \mathbf{k}_2}^e \right]^* \quad (3.49)$$

$$H_{u_1 c_1 \mathbf{k}_1, u_2 c_2 \mathbf{k}_2}^e = - \left[H_{c_1 u_1 \mathbf{k}_1, c_2 u_2 \mathbf{k}_2}^e \right]^*. \quad (3.50)$$

The off-diagonal blocks (in Eqs. (3.48) and (3.49)) can be neglected in the Tamm-Dancoff approximation (TDA). This approximation is valid in the optical limit if the binding energies of the excitations are small compared to the band gap [49]. In this work, we consider X-ray absorption spectroscopy in the optical limit where the energy difference between core and conduction states is typically several hundred eV, whereas binding energies are typically on the order of a few eV. We assume the TDA to be valid in this work. We note, however, that its validity for X-ray absorption spectroscopy is not thoroughly explored. The Hamiltonian H_e then splits into two block-diagonal parts. Additionally, only the Hermitian first block in Eq. (3.47) has to be calculated because its eigenvalues and eigenvectors uniquely define the eigenvalues and -vectors of Eq. (3.50). The eigenvalue problem with the eigenvectors $A_{c\mathbf{k}}^\lambda$ can be expressed as:

$$\sum_{c' u' \mathbf{k}'} H_{c\mathbf{k}, c' u' \mathbf{k}'}^{BSE} A_{c' u' \mathbf{k}'}^\lambda = E^\lambda A_{c\mathbf{k}}^\lambda. \quad (3.51)$$

The eigenvectors represent the expansion coefficients of the excitonic wavefunction $\Phi^\lambda(\mathbf{r}, \mathbf{r}')$ with transition energy E^λ in the single-particle wavefunction of electron and hole:

$$\Phi^\lambda(\mathbf{r}_e, \mathbf{r}_h) = \sum_{c\mathbf{k}} A_{c\mathbf{k}}^\lambda \psi_{c\mathbf{k}}(\mathbf{r}_e) \psi_{c\mathbf{k}}(\mathbf{r}_h)^*. \quad (3.52)$$

⁶Note that the indices $i_1 \dots i_4$ have been explicitly expressed as band indices.

Here, \mathbf{r}_e and \mathbf{r}_h are the positions of the excited electron and hole, respectively. Knowing the solution of the eigenvalue problem and using the spectral theorem, the two-particle correlation function L can be expressed as:

$$L_{c_1 u_1 \mathbf{k}_1, c_2 u_2 \mathbf{k}_2} = -i \sum_{\lambda} \frac{A_{c_1 u_1 \mathbf{k}_1}^{\lambda} [A_{c_2 u_2 \mathbf{k}_2}^{\lambda}]^*}{E^{\lambda} - \omega}. \quad (3.53)$$

The transition coefficients t_{λ} are calculated as

$$t_{\lambda} = \sum_{c u \mathbf{k}} A_{c u \mathbf{k}}^{\lambda} \frac{\langle c \mathbf{k} | \hat{\mathbf{p}} | u \mathbf{k} \rangle}{\epsilon_{u \mathbf{k}} - \epsilon_c}, \quad (3.54)$$

where $\epsilon_{u \mathbf{k}}$ and ϵ_c are the single-particle energies of the conduction and core state, respectively, and $\langle c \mathbf{k} | \hat{\mathbf{p}} | u \mathbf{k} \rangle$ the momentum matrix elements between both states. Then, the imaginary part of the dielectric tensor is obtained as

$$\text{Im } \epsilon_M(\omega) = \frac{8\pi^2}{\Omega} |t_{\lambda}|^2 \delta(\omega - E_{\lambda}). \quad (3.55)$$

The effective Hamiltonian H^{BSE} is calculated using Eq. (3.47)

$$H_{c u \mathbf{k}, c' u' \mathbf{k}'}^e = (\epsilon_{u \mathbf{k}} - \epsilon_c) \delta_{cc'} \delta_{uu'} + i \Xi_{c u \mathbf{k}, c' u' \mathbf{k}'}, \quad (3.56)$$

where the interaction kernel Ξ is defined by Eq. (2.41) as:

$$\Xi_{(i_1 i_2), (i_3 i_4)} = \int d^3 r_1 d^3 r_1' d^3 r_2 d^3 r_2' \psi_{i_1}(\mathbf{r}_1) \psi_{i_2}^*(\mathbf{r}_1') \psi_{i_3}^*(\mathbf{r}_2) \psi_{i_4}(\mathbf{r}_2') \Xi(\mathbf{r}_1, \mathbf{r}_1', \mathbf{r}_2, \mathbf{r}_2'). \quad (3.57)$$

The interaction kernel and two-particle correlation function are expanded in single-particle wavefunctions in section 2.3. In that derivation, the characters of the single-particle states are neglected. The spin index $\sigma = 1, 2$ for spin-up and spin-down states is introduced in the following. The use of spinorial states ensures the inclusion of spin-orbit coupling for the description of core states.

The effective Hamiltonian can be separated

$$H^{BSE} = H^{diag} + H^x + H^c, \quad (3.58)$$

where H^{diag} is the diagonal contribution

$$H_{c u \mathbf{k}, c' u' \mathbf{k}'}^{diag} = (\epsilon_{u \mathbf{k}} - \epsilon_c) \delta_{cc'} \delta_{uu'} \delta_{\mathbf{k} \mathbf{k}'}. \quad (3.59)$$

H^x is the repulsive exchange part and contains the short-range part of the bare Coulomb potential $\bar{v}(\mathbf{r}, \mathbf{r}')$:

$$H_{c u \mathbf{k}, c' u' \mathbf{k}'}^x = \int d^3 r d^3 r' \sum_{\sigma} \psi_{c \mathbf{k} \sigma}(\mathbf{r}) \psi_{u \mathbf{k} \sigma}^*(\mathbf{r}) \bar{v}(\mathbf{r}, \mathbf{r}') \sum_{\sigma'} \psi_{c' \mathbf{k}' \sigma'}^*(\mathbf{r}') \psi_{u' \mathbf{k}' \sigma'}(\mathbf{r}'). \quad (3.60)$$

H^c is the attractive direct part and contains the screened Coulomb interaction $W(\mathbf{r}, \mathbf{r}')$:

$$H_{c u \mathbf{k}, c' u' \mathbf{k}'}^c = - \int d^3 r d^3 r' \sum_{\sigma} \psi_{c \mathbf{k} \sigma}(\mathbf{r}) \psi_{c' \mathbf{k}' \sigma}^*(\mathbf{r}) W(\mathbf{r}, \mathbf{r}') \sum_{\sigma'} \psi_{u \mathbf{k} \sigma'}^*(\mathbf{r}') \psi_{u' \mathbf{k}' \sigma'}(\mathbf{r}'). \quad (3.61)$$

The BSE Hamiltonian in X-ray absorption spectroscopy can be separated into atomic contributions [14]. The imaginary part of the macroscopic dielectric function can therefore also be expressed as a sum of the individual atomic contributions

$$\text{Im } \epsilon_M = \sum_{\alpha} \text{Im } \epsilon_M^{\alpha}, \quad (3.62)$$

where α represents the different atoms. In this work, we calculate the contributions to the dielectric function by the individual atoms of the unit cell.

3.2 Description of Core States

In the previous section we introduced the importance of treating accurately spinorial states to correctly describe core states. The Dirac equation determines electron energies and wavefunctions, and includes relativistic corrections such as the spin-orbit coupling. Core states are tightly bound and strongly localized around the corresponding atoms. As a result, the respective potentials are assumed to be spherically symmetric. The full Dirac equation can be thus transformed into a set of coupled radial equations. Since the Dirac Hamiltonian commutes with the total angular momentum operator $\hat{\mathbf{J}} = \hat{\mathbf{L}} + \hat{\mathbf{S}}$, the Dirac equation can be separated into a radial and spherical part. The spherical part consists of spin spherical harmonics, namely the eigenfunctions of \mathbf{J}^2 and J_z . They are constructed from two-dimensional spinors, which are eigenfunctions of \mathbf{S}^2 and S_z , and from the spherical harmonics, the eigenfunctions of \mathbf{L}^2 and L_z . The spin spherical harmonics $\Omega_{(l,s)j,M}$ are defined as:

$$\Omega_{(l,\frac{1}{2})l+\frac{1}{2},M}(\hat{r}) = \begin{pmatrix} \sqrt{\frac{l+M+\frac{1}{2}}{2l+1}} Y_{l,M-\frac{1}{2}}(\hat{r}) \\ \sqrt{\frac{l-M+\frac{1}{2}}{2l+1}} Y_{l,M+\frac{1}{2}}(\hat{r}) \end{pmatrix}, \quad (3.63)$$

and

$$\Omega_{(l,\frac{1}{2})l-\frac{1}{2},M}(\hat{r}) = \begin{pmatrix} -\sqrt{\frac{l-M+\frac{1}{2}}{2l+1}} Y_{l,M-\frac{1}{2}}(\hat{r}) \\ \sqrt{\frac{l+M+\frac{1}{2}}{2l+1}} Y_{l,M+\frac{1}{2}}(\hat{r}) \end{pmatrix}. \quad (3.64)$$

The 4-component Dirac wavefunction is then written as [50]:

$$\psi_{\kappa,M}(\mathbf{r}) = \begin{pmatrix} u_{\kappa}(r) \Omega_{\kappa,M}(\hat{r}) \\ -iv_{\kappa}(r) \Omega_{-\kappa,M}(\hat{r}) \end{pmatrix}. \quad (3.65)$$

where $u_{\kappa}(r)$ and $-iv_{\kappa}(r)$ are the radial functions for the *large* and *small* component, respectively. The quantum number κ is introduced as a unique index for a state $(l, s)j, M$:

$$\kappa = \begin{cases} -l - 1, & J = l + \frac{1}{2} \\ l, & J = l - \frac{1}{2} \end{cases}. \quad (3.66)$$

The radial functions are determined by the coupled radial Dirac equations [51]:

$$\frac{\partial u_\kappa}{\partial r} = \frac{1}{c} (v_{\text{KS}}^s - \epsilon_\kappa) v_\kappa + \left(\frac{\kappa - 1}{r} \right) u_\kappa \quad (3.67)$$

$$\frac{\partial v_\kappa}{\partial r} = - \left(\frac{\kappa + 1}{r} \right) v_\kappa + 2c \left[1 + \frac{1}{2c^2} (\epsilon_\kappa - v_{\text{KS}}^s) \right]. \quad (3.68)$$

The non-relativistic conduction states are obtained as solutions of the scalar-relativistic Hamiltonian. In order to compute matrix elements between core and conduction states, the *small* component of the core states is neglected [11, 14]. The core wavefunction for a given atom α at position \mathbf{R}_α then takes on the form:

$$\psi_{\kappa,M}(\mathbf{r}) = \begin{cases} u_\kappa(r) \Omega_{\kappa,M}(\hat{\mathbf{r}}), & r_\alpha \leq R_{\text{MT}} \\ 0, & \mathbf{r} \in I \end{cases}. \quad (3.69)$$

3.3 Description of Conduction States

Conduction states are calculated by a full potential all-electron DFT calculation using the (L)APW+lo basis set. They are treated in the zero-order regular approximation (ZORA) [52] to the Dirac equation without the spin-orbit coupling term, thereby taking into account relativistic effects within the muffin-tin spheres. The Kohn-Sham Hamiltonian within the muffin-tin spheres can then be written as:

$$h^{\text{ZORA}} = \mathbf{p} \frac{1}{1 - \frac{v_{\text{KS}}^s}{2c^2}} \mathbf{p} + v_{\text{KS}}, \quad (3.70)$$

where v_{KS}^s is the spherically averaged effective Kohn-Sham potential. For the many-body calculations, the Kohn-Sham wavefunctions $\psi_{i\mathbf{k}}(\mathbf{r})$ of atom α are expanded in a basis of spherical harmonics within the muffin-tin sphere:

$$\psi_{i\mathbf{k}}^\alpha = \sum_{lm} u_{lm}^{i\mathbf{k}}(r_\alpha) Y_{lm}(\hat{\mathbf{r}}_\alpha). \quad (3.71)$$

Here, the radial function is given in the (L)APW+lo basis by Eq. (1.23). Since we want to calculate matrix elements between spinorial core states and conduction states, an approximation of the spinorial character of the conduction states is required. In this work, we assume an average contribution between the two-spin channels [14]:

$$\psi_{i\mathbf{k}}^{\text{spinor}} = \begin{pmatrix} \frac{1}{\sqrt{2}} \\ \frac{1}{\sqrt{2}} \end{pmatrix} \psi_{i\mathbf{k}}. \quad (3.72)$$

As a result of this approximation, we can employ spin-unpolarized DFT calculations as a starting point for the X-ray absorption spectroscopy calculations.

4 X-Ray Absorption Spectroscopy

X-Ray Absorption Spectroscopy (XAS) measures the absorption coefficient near the absorption edge of an element as a function of X-ray energy. Beer's Law defines the energy-dependent X-ray absorption coefficient $\mu(E)$, by relating the incoming intensity I_0 of X-ray beams to the transmitted intensity I_t behind a sample of thickness d :

$$I_t(d) = I_0 e^{-\mu(E)d}. \quad (4.73)$$

In Fig. 3.2, a schematic view of the X-ray absorption coefficient $\mu(E)$ as a function of incidence photon energy E is displayed. We can identify three main features: (1) The overall smooth decrease of $\mu(E)$, (2) the occurrence of sharp peaks known as absorption edges, and (3) small oscillations near the absorption edges.

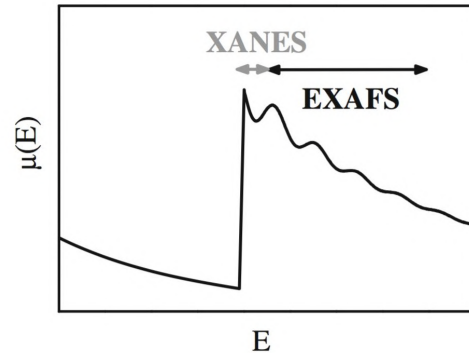


Figure 3.2: Schematic view of the X-ray absorption coefficient $\mu(E)$ as a function of incidence photon energy E . Figure taken from [53].

The overall decrease of the absorption coefficient is due to the background absorption of the atoms. The absorption edges reflect the transition of a bound core electron to an unoccupied state. As listed in Tab. III.1, they are commonly denoted by their initial atomic state.

Table III.1: Notation for X-ray absorption edges. Listed are the three deepest atomic states.

Absorption edge	Initial atomic state
K	$1s_{1/2}$
L_1	$2s_{1/2}$
$L_{2,3}$	$2p_{1/2}, 2p_{3/2}$

The oscillations above the absorption edges are known as the X-ray absorption fine structure (XAFS). Two regions are commonly distinguished: the X-ray absorption near edge structure (XANES)⁷, usually about 30 eV above the absorption edge, and the extended X-ray absorption fine structure (EXAFS), the region beyond the XANES. Transitions to bound unoccupied states characterize the region close to the absorption edge. XANES is therefore sensitive to

the chemical environment of the probed atom and can be used to detect the presence of specific bonds in molecules, such as C–C and C=C bonds in organic materials, determine intra-molecular bond lengths, and derive the orientation of molecules in solids or on surfaces [9]. EXAFS is characterized by transitions from the core electron to free or continuous unoccupied states and is able to reveal the local structure of the sample [54,55]. In this work we are only interested in the XANES region.

The polarization dependence of the K absorption edge is commonly used to probe

⁷XANES is also known as near edge X-ray absorption fine structure (NEXAFS)

the amplitude and directionality of the molecular orbitals on the excited atom [9], as well as the orientation of an organic material on a substrate [17, 56, 57]. In this work, the σ^* and π^* resonances are of particular interest for the carbon K and sulfur K absorption edges of the investigated systems. They can be described as dipole transitions from the $1s$ initial state to the p component of the final state. When we assume a constant resonance shape and only a change in peak height, the change in resonance intensity is proportional to the change in oscillator strength. The intensity can then be expressed as

$$I \propto |\langle f | \mathbf{e} \cdot \mathbf{p} | i \rangle|^2 \quad (4.74)$$

using Fermi's golden rule. Here, \mathbf{e} is the unit electric field vector, \mathbf{p} the transition dipole moment, i the $1s$ initial state, and f the molecular orbital final state.

In an aromatic heterocyclic molecule such as thiophene, the spatial orientation of the σ^* orbitals can be represented by the plane spanned by the atoms and the π^* orbitals by a vector perpendicular to this plane. This is illustrated for the 2T molecule in Fig. 3.3. For a transition from the spherically symmetric $1s$ state to a π^* orbital created by linearly polarized light, the matrix element $|\langle f | \mathbf{e} \cdot \mathbf{p} | i \rangle|$ points in the direction of the π^* orbital \mathbf{O} and simplifies to [58]:

$$I \propto |\mathbf{e} \cdot \langle f | \mathbf{p} | i \rangle|^2 \propto \cos^2 \delta. \quad (4.75)$$

Here, δ is the angle between the electric field vector \mathbf{E} and the direction of the π^* orbital \mathbf{O} . Analogously, one can derive the expression for a transition to a σ^* state as [58]

$$I \propto \sin^2 \gamma, \quad (4.76)$$

where γ is the angle between \mathbf{E} and the normal \mathbf{n} of the molecular plane. Equations 4.75 and 4.76 lead to a simple description of the dipole selection rules for K absorption edges: *The resonance intensity associated with a molecular orbital final state is at its maximum if \mathbf{E} points in the direction of the orbital, and it vanishes if \mathbf{E} is perpendicular to the direction [9].*

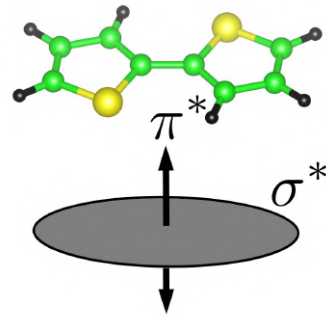


Figure 3.3: Schematic illustration of the spatial orientation of σ^* and π^* orbitals for the bithiophene molecule.

IV Computational Parameters

All calculations in this work are performed using the full-potential all-electron **exciting** code [15] for DFT and MBPT calculations. In the framework of the (L)APW+lo method, we treat the $1s$, $2s$, and $2p$ states of sulfur, and the $1s$ state of carbon as core states. The XAS spectra are calculated via the solution of the BSE as implemented in the **exciting** code [11, 14].

As a starting point for the BSE, the Kohn-Sham electronic structure is computed within the local-density approximation (Perdew-Wang functional) [34]. Converging the total energy leads to the employed computational parameter set: a $8 \times 8 \times 6$ k -grid and a planewave cut-off $R_{\text{MT}}^{\text{min}} G_{\text{max}} = 5.0$ for 2T, a $3 \times 5 \times 2$ k -grid and $R_{\text{MT}}^{\text{min}} G_{\text{max}} = 5.0$ for 4T, and a $3 \times 5 \times 1$ k -grid and $R_{\text{MT}}^{\text{min}} G_{\text{max}} = 5.0$ for 6T. Muffin-tin spheres R_{MT} of $1.2 a_0$ for C, $0.8 a_0$ for H, and $2.0 a_0$ for S are considered. Quasiparticle energies are approximated by the Kohn-Sham single-particle energies, and thus we expect the absorption onset to be underestimated by about 10%. A scissors operator is therefore applied to align the calculated spectra to experimental references when available. This is a common practice for theoretical XAS results. [11, 16]

For the calculation of the carbon K absorption edge, we adopt a $6 \times 6 \times 4$ k -grid and a planewave cut-off $R_{\text{MT}}^{\text{min}} G_{\text{max}} = 4.5$ for 2T, a $3 \times 5 \times 2$ k -grid and $R_{\text{MT}}^{\text{min}} G_{\text{max}} = 4.0$ for 4T, and a $8 \times 8 \times 6$ k -grid and $R_{\text{MT}}^{\text{min}} G_{\text{max}} = 4.0$ for 6T. Local-field effects for the C K absorption edge are treated for a cut-off $|\mathbf{G} + \mathbf{q}|_{\text{max}}$ of $4.5 a_0^{-1}$ for 2T, $3.0 a_0^{-1}$ for 4T, and $3.0 a_0^{-1}$ for 6T. The screening of the Coulomb potential is calculated in the random phase approximation, including all valence bands and 200 unoccupied states. 50, 70, and 60 unoccupied states are included in the diagonalization of the BSE for the C K absorption edge for 2T, 4T, and 6T, respectively.

The absorption spectrum from the sulfur K edge is performed for a $6 \times 6 \times 4$ k -grid and a planewave cut-off $R_{\text{MT}}^{\text{min}} G_{\text{max}} = 4.5$ for 2T, a $3 \times 5 \times 2$ k -grid and $R_{\text{MT}}^{\text{min}} G_{\text{max}} = 4.0$ for 4T, and a $3 \times 5 \times 2$ k -grid and $R_{\text{MT}}^{\text{min}} G_{\text{max}} = 4.0$ for 6T. Local-field effects are included with a cut-off $|\mathbf{G} + \mathbf{q}|_{\text{max}}$ of $4.5 a_0^{-1}$ for 2T, $3.5 a_0^{-1}$ for 4T, and $3.5 a_0^{-1}$ for 6T. The screening of the Coulomb potential is computed for all valence bands and 200 unoccupied states. The diagonalization of the BSE includes 100, 120, and 120 unoccupied states for 2T, 4T, and 6T, respectively.

For the sulfur $L_{2,3}$ absorption edge calculation, a $4 \times 4 \times 4$ k -grid and a planewave cut-off $R_{\text{MT}}^{\text{min}} G_{\text{max}} = 4.5$ for 2T, a $3 \times 5 \times 2$ k -grid and $R_{\text{MT}}^{\text{min}} G_{\text{max}} = 4.0$ for 4T, and a $3 \times 5 \times 2$ k -grid and $R_{\text{MT}}^{\text{min}} G_{\text{max}} = 4.0$ for 6T is adopted. A cut-off $|\mathbf{G} + \mathbf{q}|_{\text{max}}$ of $5.0 a_0^{-1}$ for 2T, $3.0 a_0^{-1}$ for 4T, and $3.0 a_0^{-1}$ for 6T is applied for the inclusion of local-field effects. The screening of the Coulomb potential is computed for all valence bands and 200 unoccupied states. The diagonalization of the BSE includes 100 unoccupied states for 2T, 100 for 4T, and 130 for 6T.

The adopted parameters ensure a convergence of the spectral shape and an accuracy of 20 meV for the lowest energy eigenvalue. If not specified otherwise, we apply an artificial Lorentzian broadening of 150 meV to all investigated absorption edges.

V Electronic Structure

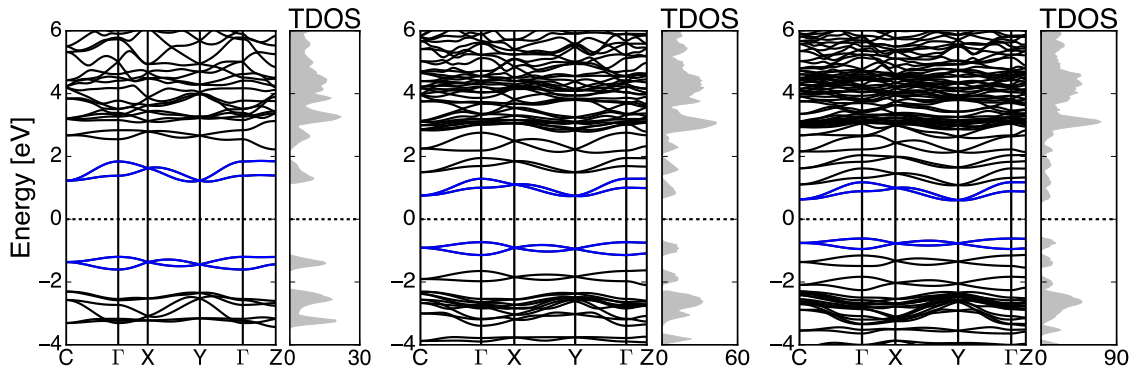


Figure 5.1: Band structure and total density of states (TDOS) around the band gap for 2T (left), 4T (middle) and 6T (right). Subbands corresponding to the uppermost valence band pair and lowest conduction band pair are in blue. Energies are relative to the Fermi level, in the mid gap, marked by the dotted line.

X-ray absorption spectra are highly dependent on the local electronic structure of the absorbing atoms. The quantum-mechanical selection rules determine the spectral features: dipole allowed transitions ($\Delta l = \pm 1$) from core to conduction states produce the spectral features. The analysis of the electronic structure in terms of the band structure and density of states is therefore crucial for interpreting the XAS. In the following, the conduction states are discussed since they are probed by XAS.

Band structures are calculated along high-symmetry points of the monoclinic unit cell. The considered high-symmetry points in units of $(2\pi/a, 2\pi/b, 2\pi/c)$ are $\Gamma = (0, 0, 0)$, $C = (0.5, 0.5, 0)$, $X = (0.5, 0, 0)$, $Y = (0, 0.5, 0)$, and $Z = (0, 0, 0.5)$. In Fig. (5.1) the band structures of crystalline 2T, 4T, and 6T around the band gap are depicted. Our results for the band structure of crystalline 4T and 6T show good agreement with previously published results obtained with the semi-empirical extended Hückel theory method [26, 28], DFT [30, 59], and experiments [59]. One characteristic feature of molecular crystals is evident: Each band is split due to the presence of two inequivalent molecules in the unit cell (see Fig. 2.2). The lowest conduction band pair (LUMO pair) and highest valence band pair (HOMO pair) are highlighted in blue. With increasing molecular length, additional subbands in the valence and conduction region appear. This is also reflected in the density of states where subbands are represented by sharp peaks. The peaks in the lower conduction bands are well separated in 2T and 4T but are overlapping in 6T. The band pairs are generally non-degenerate and exhibit band splitting except at the Brillouin zone boundaries X and Y, i.e. along the \mathbf{a}^* and \mathbf{b}^* directions. These results show good agreement with calculations performed by Klett et al. [30] for 6T crystals. The band splitting of the HOMO pair is at its maximum at the Γ point and we obtain values of 454 meV, 286 meV, and 287 meV for 2T, 4T, and 6T, respectively. The previously reported band splitting at Γ of 450 meV for 4T and 420 meV for 6T by Siegrist et al. [26, 28] is higher than ours. We attribute this difference to the different underlying theoretical approaches, i.e. *ab-initio* DFT versus the semi-empirical quantum chemistry approach. The largest band dispersion for the HOMO pair is along the ΓC , ΓX , and ΓY paths. These paths can be related to the geometrical axes in the

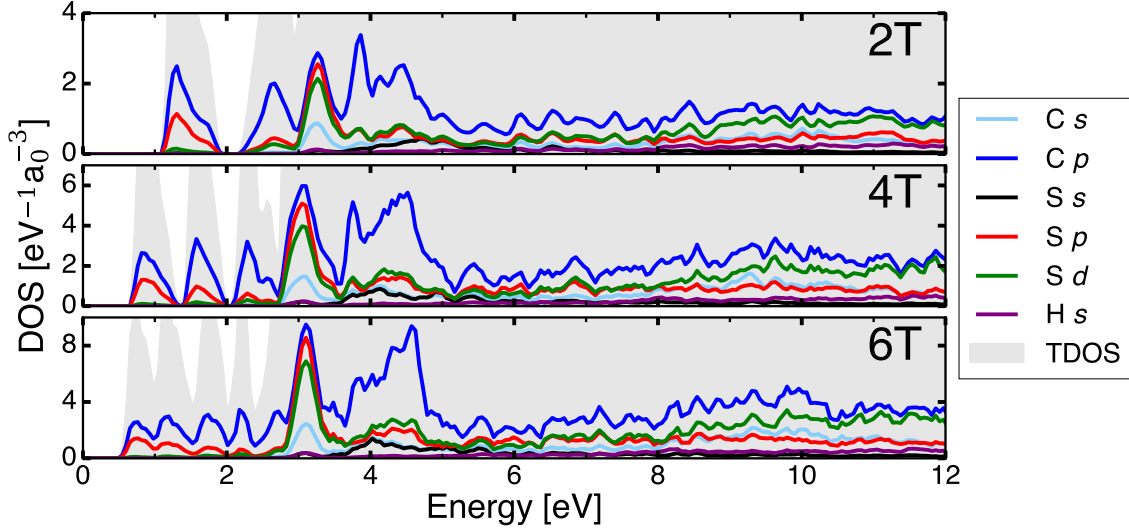


Figure 5.2: Projected density of states for hydrogen, carbon, and sulfur atoms in 2T (top), 4T (middle) and 6T (bottom). The grey area represents the total density of states and energies are relative to the Fermi level.

unit cell: the path along $\overline{\Gamma\text{C}}$ is in the $\mathbf{a}^*\mathbf{b}^*$ plane, and $\overline{\Gamma\text{X}}$ ($\overline{\Gamma\text{Y}}$) is parallel to the \mathbf{a}^* (\mathbf{b}^*) axis. Minimal dispersion can be found along the $\overline{\Gamma\text{Z}}$ path which is parallel to the \mathbf{c}^* axis and represents approximately the long molecular axis. In summary, the band dispersion is largest along directions that are perpendicular to the long molecular axis and minimal along directions parallel to it (see also Fig. 2.2 and Tab. II.1). Charge-carrier mobilities are therefore expected to be the highest in directions in the $\mathbf{a}^*\mathbf{b}^*$ plane regardless of oligomer length. Our findings are supported by previously published results for 4T [26] and 6T [28, 30, 59] crystals. Similar results have also been found in other molecular crystals, such as in oligoacene [60] and sexiphenyl crystals [61]. The overall flat band character of the conduction states around the band gap can be attributed to the dominant role of the organic p orbitals.

The projected density of states (PDOS) of the conduction bands is shown in Fig. 5.2. The lower lying conduction bands up to 3 eV are represented by sharp peaks. These peaks have mainly C p and S p character and are formed by the antibonding π^* orbitals of the oligothiophene molecules. The LUMO subbands are formed by π^* orbitals, as illustrated in Appendix B, and therefore are expected to contribute significantly to the C K -edge and S K -edge absorption spectra. The contribution from the C p states is similar for all subbands below 3 eV, while that of the S p states is decreasing when going to higher energy bands. Additionally, there are also small contributions from S d states. This hybridization with S d states, while seemingly insignificant, plays a crucial part in explaining the aromatic character of oligothiophene [62] as well as its electronic structure [63]. The LUMO subbands should therefore also contribute to the S $L_{2,3}$ absorption edge. The DOS of all investigated systems has its strongest peak at approximately 3 eV where multiple hybridized states contribute (see also Fig. 5.1) including the $\sigma^*(\text{C-S})$, the $\sigma^*(\text{C-C})$, and the $\sigma^*(\text{C-H})$ orbitals. As a result of this hybridization, we expect significant contributions from these bands to all investigated absorption edges. The region from 3.5 eV

to 5 eV has mainly C p character and can be attributed to higher lying $\sigma^*(\text{C-C})$ orbitals with small contributions from S d , S p , S s , and C s states. From 5 eV to 8 eV we find hybridized states of S p , S d , and C p states character. At energies above 8 eV, the DOS is dominated by hybridized C p - S d states with contributions from C s and S p states. The overall PDOS is very similar for all investigated systems. The main differences are the occurrence of additional bands and a slight red shift of the strongest peak with increasing oligomer length. Additionally, from 3 eV to 5 eV, the contribution from C p states shifts to higher energies with increasing oligomer length.

VI XANES of Oligothiophene Crystals

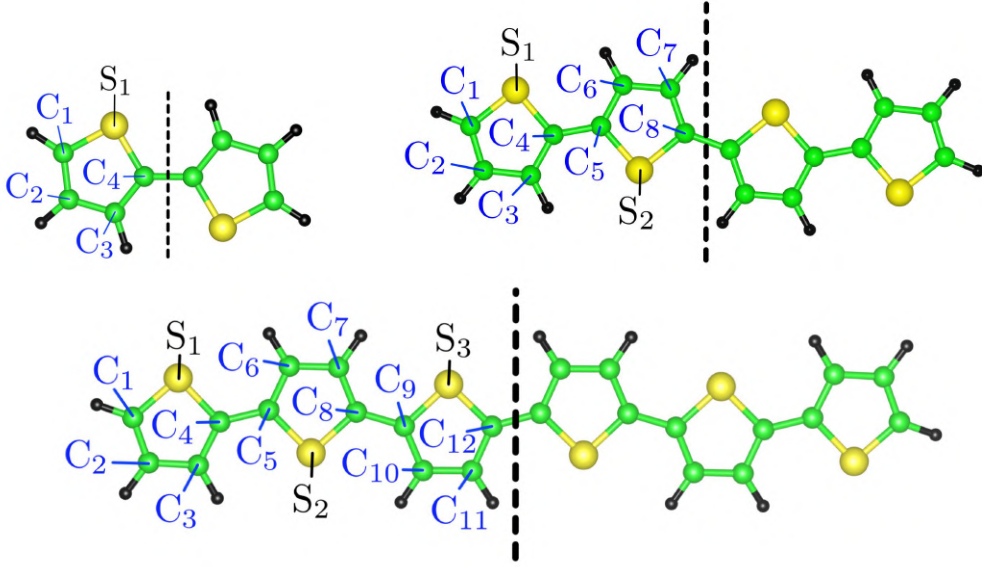


Figure 6.1: Nomenclature for the inequivalent atoms in 2T, 4T, and 6T oligomers. The black dotted line indicates the reflection symmetry of the oligomer.

In this chapter, we present our results for the carbon K , sulfur K , and sulfur $L_{2,3}$ absorption edges of n T crystals. The absorption edges are calculated for all inequivalent atoms in the unit cells. The adopted nomenclature is illustrated in Fig. 6.1. We find that the atoms on one half of the molecule are equivalent to the corresponding atoms on the other half. It is therefore sufficient to calculate the absorption spectra for only one half of the oligomer. The spectra of both inequivalent molecules in the unit cell are identical. The numerical equivalence was tested for several parameter sets and spectra were found to be identical in all cases.

The different absorption edges are primarily discussed for one oligothiophene crystal: The C K edge and S $L_{2,3}$ edge are presented for 2T and the S K edge for 4T. We then analyze the similarities and the differences for increasing oligomer length n .

As discussed in Chapter III, we are interested in the imaginary part of the macroscopic dielectric tensor. Its number of inequivalent components depends on the crystal symmetry. All investigated oligothiophenes crystallize in a monoclinic structure, thereby reducing the number of independent components to four. The macroscopic dielectric tensor then assumes the form:

$$\epsilon_M = \begin{pmatrix} \epsilon_{xx} & 0 & \epsilon_{xz} \\ 0 & \epsilon_{yy} & 0 \\ \epsilon_{xz} & 0 & \epsilon_{zz} \end{pmatrix}.$$

Every excitation energy of the isolated molecule gives rise to two non-degenerate bands of excited states for the corresponding crystal structure. The cause of this splitting is the presence of two inequivalent molecules in the unit cell: The transition dipole moments for both molecules are not oriented parallel to each other, thus

giving rise to two non-degenerate excited states with orthogonal polarizations [64]. This is known as the Davydov splitting in molecular crystals [64]. Excitations from the K absorption edge of nT crystals lead to the formation of a bright exciton with large oscillator strength and a dark exciton with almost vanishing oscillator strength. In the case of the $L_{2,3}$ absorption edge, excitations generate several excitons with non-vanishing oscillator strength.

1 Carbon K Absorption Edge

The C K absorption edge of molecular crystals is commonly investigated to determine the orientation of the molecules on a substrate [9]. Oligothiophenes have been studied experimentally and theoretically in this context: HT-2T/4T monolayers on metal surfaces are typically oriented with their molecular planes parallel to the substrate [17–19] while 6T thin films adopt a more upright geometry on glass substrates [57]. The effect of long chain oligomers on the spectral features, however, is not well explored and has only recently been studied for short chains up to 3T in the gas phase [20]. Additionally, the assignment and the analysis of the C K absorption edge is well explored for the thiophene monomer but is increasingly difficult for longer chains with the appearance of additional bands in the electronic structure. With this work, we further supplement experimental XAS from the C K absorption edge with an analysis of spectral features and bound excitons for oligothiophenes up to 6T. Our *ab-initio* approach enables us to accurately determine the origin of spectral features. Additionally, we identify similarities and differences for increasing oligomer length.

1.1 Analysis of XAS of Crystalline 2T

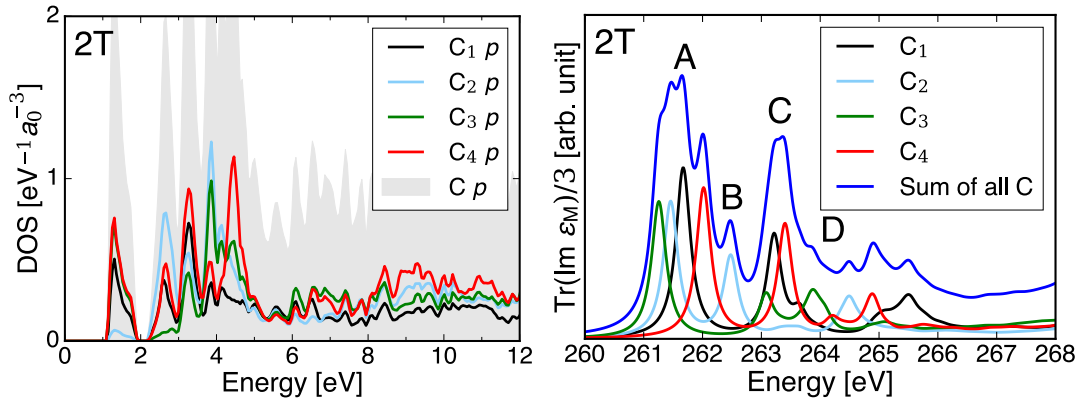


Figure 6.2: Left: Projected density of states of the C p states of 2T. The grey area represents the sum of all inequivalent C p contributions. Energies are relative to the Fermi level (set to zero in the mid-gap). Right: Absorption spectra from the C K edge of 2T. Shown is the solution of the BSE for the inequivalent C atoms as the average over the diagonal Cartesian components of the imaginary part of the macroscopic dielectric tensor. The blue line denotes the contributions from all inequivalent C atoms.

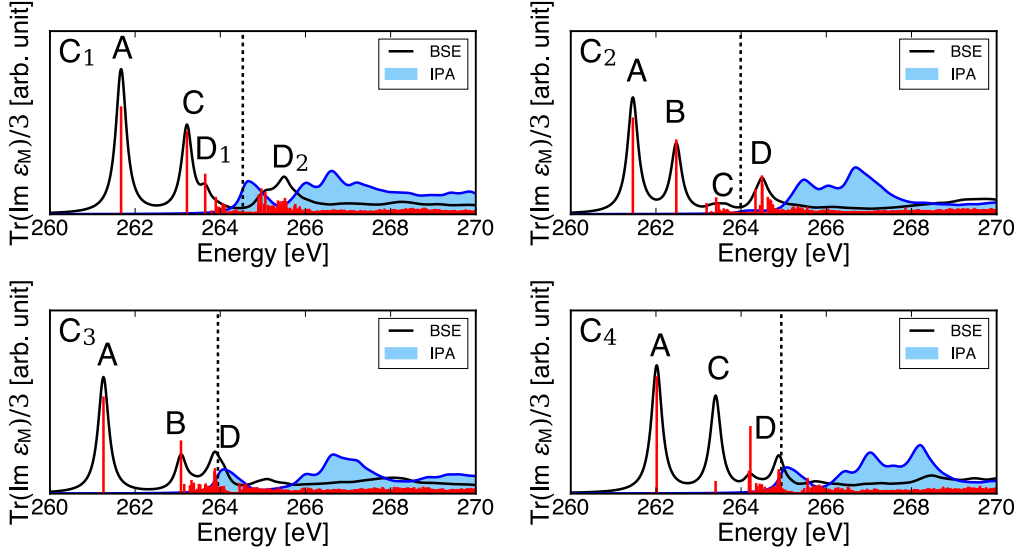


Figure 6.3: Absorption Spectra from the C K -edges considering inequivalent C atoms in 2T. Excitation energies (red vertical bars) and their oscillator strength indicated by the height of the bars for a BSE calculation. Solutions of the BSE and the independent particle approximation (IPA) are in black and blue, respectively. The dashed line represents the independent particle onset.

We start our analysis of the C K absorption edge by comparing the IPA and BSE solutions for 2T crystals. In Fig. 6.3, we show the spectra obtained from the inequivalent C K absorption edges as an average of the diagonal Cartesian components. The IPA spectrum is proportional to the PDOS of the conduction states, weighted by the momentum matrix elements between core and conduction states, $\langle \mathbf{c}\mathbf{k} | \hat{\mathbf{p}} | u\mathbf{k} \rangle$. Since transitions to states with p orbital character are dipole-allowed, we can relate the C p PDOS, shown in Fig. 6.2, with the obtained IPA spectra.

The first peak at the IP onset represents transitions to the LUMO subbands. Note that this peak is weak for C_2 , because the LUMO subbands are not localized on this atom (see Appendix B). Beyond the first peak, the IPA spectrum is reflected by the p PDOS of the inequivalent C atoms: A broader band of excitons with a bandwidth of about 3 eV to 4 eV is found above the first peak. They are formed by transitions to the bands in the range from 2.0 eV to 5.0 eV. Here, the second peak corresponds to transitions to the LUMO+1 subbands with π^* character. This peak is less intense for C_3 because of its small p orbital contribution to these bands. For the C atoms with a bond to a sulfur atom (C_1 , C_4), we find a pronounced third peak at 3.2 eV representing transitions to bands with σ^* character associated with the S-C bond. At energies higher than 5.0 eV, the PDOS does not exhibit any pronounced peaks but oscillates around a value of about $0.4 \text{ eV}^{-1} a_0^{-3}$.

The inclusion of the attractive electron-hole interaction in the BSE shifts the absorption to lower energy by more than 2.5 eV and leads to a significant redistribution of oscillator strength to a few excitons (see Fig. 6.3). Local field effects (LFE) do not play a major role in the formation of the excitons (for details see Appendix B). By comparing singlet and triplet excitations, we obtain differences between the excitation energies of less than 150 meV which undermines the predominant role of the

screened Coulomb interaction for the XAS. This is a result of the highly localized character of the excitons and has previously been found for the nitrogen K absorption edge of azobenzene monolayers [16]. LFE play a more dominant role in optical excitations of nT crystals where the singlet-triplet splitting is of the same order than the binding energies [65].

We can identify several peaks in the BSE spectrum that are redshifted compared to the IPA features. Our labeling of the peaks is indicated on the right side of Fig. 6.2. The first peak A is formed by transitions to the LUMO subbands with C-S hybridized π^* character and covers a range from 261.3 eV to 262 eV. It is dominated by an exciton with large oscillator strength. Since all C atoms contribute to the aromatic character of 2T, this feature is present in all spectra (see Fig. 6.3). Although it is weak in the IPA spectrum of C₃, it is dominant in the corresponding BSE spectrum. Here, it is formed by transitions with π^* character to the LUMO and LUMO+1 subbands. According to our DFT calculations, the $1s$ core levels of the four inequivalent C atoms are separated by 1 eV which is comparable to the difference of 0.8 eV between the excitation energies of the A peaks. We can further distinguish two types of C atoms: C atoms with a covalent bond to S, called α -C, and C atoms without such a bond, called β -C. The shift of the α -C atoms to higher excitation energies is consistent with the higher electronegativity of sulfur compared to carbon. The largest excitation energy of peak A is found for the C₄ atom which connects the two thiophene monomers in 2T and is not bound to a hydrogen atom. Our results reproduce a trend that was previously observed for polycyclic aromatic hydrocarbons where C atoms bound to hydrogen have lower excitation energies than C atoms without such bonds [66]. Similar results were found for 2T in the gas phase using the half core hole approximation [20]. The β -C atoms, C₂ and C₃, also exhibit lower exciton binding energies of $E_b = 2.66$ eV and $E_b = 2.88$ eV compared to the α -C atoms, C₁ and C₄, with $E_b = 3.01$ eV and $E_b = 3.06$ eV for peak A. Here, we define the binding energy of the lowest lying exciton as the difference to the IPA counterpart of peak A, i.e. the IP onset. Such binding energies are typical for Frenkel excitons in molecular crystals [16, 67]. They are significantly larger than in the optical excitations of oligothiophene crystals, which are typically below 1 eV [65]. The splitting of the lowest lying excitons ranges from 152 meV for C₁ to 125 meV for C₃. These values are smaller than the reported Davydov splitting for oligothiophene crystals of 0.3 eV to 1.0 eV [68, 69] and are an indication of the reduced role of intermolecular interactions in XAS.

The second peak B at 262.5 eV originates from the β -C atoms and is dominated by an exciton with large oscillator strength. It is of π^* character and formed by transitions to the LUMO and LUMO+1 subbands for C₂ whereas it is solely formed by transitions to the LUMO+1 subbands for C₃. The third peak C from 263.2 eV to 263.4 eV is attributed to states associated with the S-C bond of the α -C atoms. It is formed by transitions to bands from 3.0 eV to 3.5 eV of σ^* character, see also the PDOS of 2T in Fig. 6.2. Additionally, there are small contributions of delocalized excitons with σ^* character from C₂. Lastly, we observe the peak structure D with contributions from all C atoms where many transitions with mixed σ^* and π^* character occur.

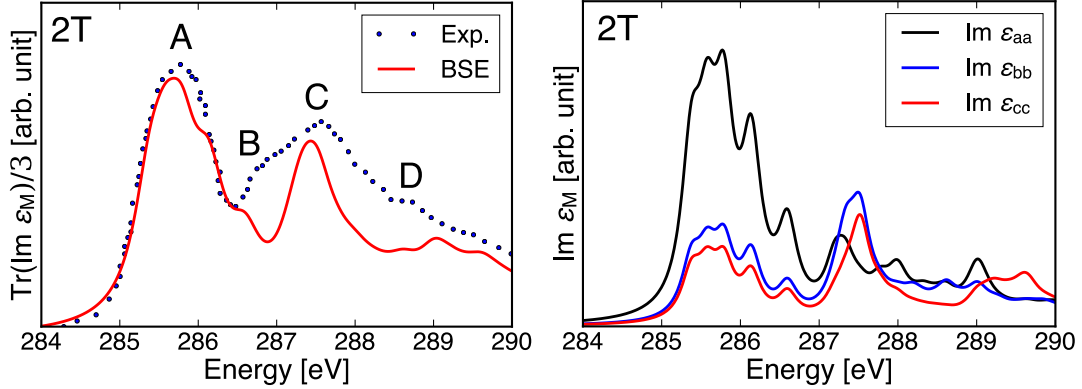


Figure 6.4: Left: Shown is the C K absorption edge of crystalline 2T including contributions from all inequivalent C atoms. The solution of the BSE is shown in red and experimental data taken from [17] is shown in blue. A Lorentzian broadening of 250 meV is applied. Right: Diagonal components of the macroscopic dielectric tensor projected on the Cartesian axes. Shown is the solution of the BSE with contributions from all inequivalent C atoms. A Lorentzian broadening of 150 meV is applied.

Our theoretical results are in very good agreement with previously published experimental data by Väterlein *et al.* for 2T multilayers on Ag(111) [17]. For comparison with experiment, we shift the absorption onset by 24.1 eV to align the spectra at the first peak. Since no information of the setup of the X-ray absorption measurement was available, we applied an average over the diagonal Cartesian components of the dielectric tensor. As shown in Fig. 6.4, we are able to accurately reproduce the four spectral features found in their results: (A) a broader resonance corresponding to transitions to the LUMO subbands, (B) a shoulder-like resonance due to transitions to the LUMO+1 subbands, (C) a third resonance due to transitions to higher bands with σ^* character associated with the α -C atoms, and (D) a shoulder they assign to higher Rydberg excitations. In our results, Peak B appears as a shoulder of peak A instead of Peak C. The relative position of peak B, however, is well replicated. Due to the limited experimental resolution, it is not possible to identify all excitonic features contributing to Peak D. The remaining peaks however are clearly resolved. It is evident that the chemical environment of the C atoms significantly alters the corresponding absorption spectrum. Additionally, we can determine that the spectra for bulk material and multilayers are directly comparable. Since the intermolecular van der Waals interaction in molecular crystals is significantly weaker than the covalent bonding within the molecules, the core excitations are strongly localized on the corresponding molecules. The spectral features are therefore mainly determined by intramolecular interactions.

On the right side of Fig. 6.4, the diagonal components of the macroscopic dielectric tensor are projected on the crystalline axes¹. We analyze the polarization dependence of the spectral features to further characterize and support our assignment of

¹The transformation from Cartesian to crystalline axes and its effect on the spectral features is detailed in Appendix A.

the resonances. Peaks A and B, formed by transitions to π^* orbitals, are primarily polarized along the a axis with only small contributions from polarizations along the b and c axes. The situation is reversed for peak C which is formed by transitions to σ^* orbitals. These results can be explained by the polarization dependence of the K absorption edge, detailed in Section III.4 : The resonances are most intense when the polarization is parallel to the direction of the final molecular orbital. As shown in Fig. 2.2, the molecular plane of 2T can be approximated by the b - c plane where c is the long molecular axis. The π^* resonances are therefore most intense for polarizations along the a axis which is perpendicular to the molecular plane. Analogously, the σ^* resonances are most intense for polarizations in the b - c plane.

1.2 Dependence on the Oligomer Length

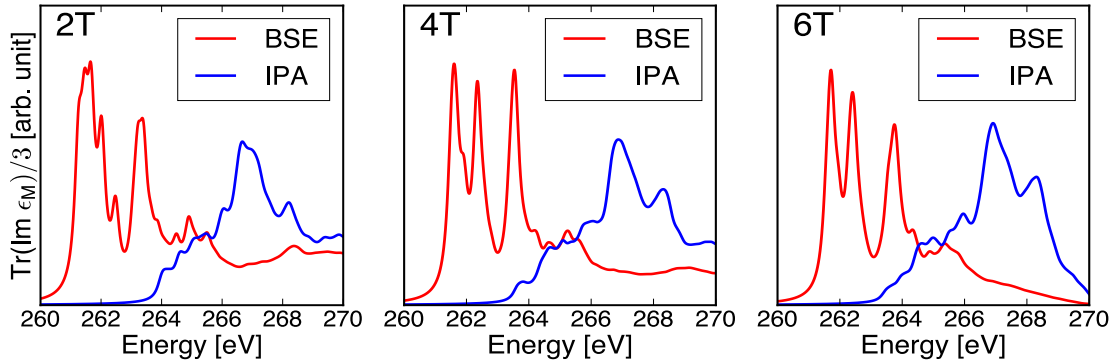


Figure 6.5: Absorption spectra from the C K absorption edge of crystalline nT from all inequivalent C atoms as the average over the diagonal Cartesian components. The red and blue lines denote the solution of the BSE and the independent particle approximation (IPA), respectively.

We now want to explore the dependence of the spectral features on the oligomer length. The BSE and IPA absorption spectra from all inequivalent C K absorption edges of nT are shown in Fig. 6.5. The overall spectral structure of the BSE and IPA solution is remarkably similar for increasing oligomer length n . The spectral features of the four inequivalent C atoms of 2T can be clearly resolved. The longer oligomers 4T and 6T contain eight and twelve inequivalent C atoms, respectively. Summing over all contributions leads to a smoother spectral shape for these crystals compared to 2T. The $1s$ core level energies of the inequivalent C atoms differ up to 0.1 eV in all investigated systems.

The most pronounced differences in the BSE spectra occur at the absorption onset in the range from 260 eV to 263 eV. Here, the π^* resonances are blueshifted for increasing oligomer length, i.e., the lowest lying excitation of 2T is shifted by 0.24 eV and 0.31 eV for 4T and 6T, respectively. In 4T and 6T, peak A is also split into two distinct peaks, A_1 and A_2 , that are separated by 0.9 eV, corresponding to the $1s$ core level energy difference. Additionally, peak B is not resolved in 4T and 6T but contributes to peak A_2 instead. We attribute the blueshift of the π^* resonances

to two effects that are commonly found in linear oligomers such as oligoacene [70]: With increasing oligomer length, the e-h pair is more delocalized and the effect of the dielectric screening is increased. This reduces the average Coulomb interaction. The effect is more pronounced when going from 2T to 4T than from 4T to 6T because the e-h pair is still mainly localized on the respective atom and does not spread over the whole length of the molecule. It is important however to distinguish where exactly the probed atom is located. The delocalization of the e-h pair decreases the closer the atom is to the edge of the molecule. This results in a shift to lower excitation energies for the atoms on the outer thiophene ring compared to inner thiophene rings (see also Fig. 6.1). Additionally, C_1 experiences a significant redshift compared to the other α -C atoms because of its additional hydrogen bond.

This effect is illustrated in Fig. 6.6 where the contributions stemming from the α - and the β -C atoms are resolved separately. We can identify a shoulder originating from C_1 between peaks A_1 and A_2 of π^* character in 4T and 6T. Peak C, however, is not significantly shifted for C_1 . With increasing oligomer length n , we are therefore able to clearly distinguish the contributions of the C atoms based on their covalent bonding to S and H atoms.

In summary, four different spectral features are found in the spectrum from the C K edge: (1) The first peak A_1 is primarily formed by transitions of the β -C atoms to the LUMO subbands. There are also contributions from higher LUMO subbands with π^* character especially for the longer molecules 4T and 6T where additional bands appear. (2) The second peak A_2 is formed by contributions from the α -C atoms with transitions primarily to the LUMO subbands. In the case of 2T, peak A and peak B are experimentally observed as the first and second peak, respectively.

For 4T and 6T, peaks B and A_2 are effectively overlapping in energy. (3) The third spectral feature C is attributed to transitions from states associated with the S-C bond of the α -C atoms. It is formed by transitions to bands with σ^* character and its excitation energy is not heavily affected by the oligomer length. The intensity of peak C in 4T is enhanced due to transitions with π^* character from the β -C atoms. (4) Lastly, we find the peak structure D which is formed by multiple transitions with mixed σ^* and π^* character. Our assignment of the spectral features for 6T

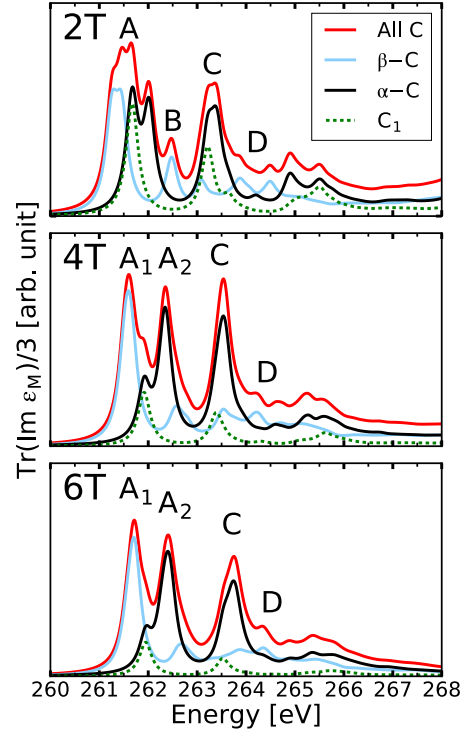


Figure 6.6: Absorption spectra from the C K absorption edge of crystalline n T. The spectral contributions of all inequivalent $\alpha(\beta)$ -C atoms are in black (lightblue). The total sum of all inequivalent C atoms is in red and the contribution from C_1 is the green dashed line.

are further supported by experimental results for 6T thin films on indium tin oxide covered glass [57]. Hörmann *et al.* resolve the aforementioned four peaks: The first two peaks are attributed to π^* resonances and the other two to σ^* resonances. In our calculations, the last peak D consists of resonances with mixed σ^* and π^* character.

Table VI.1: Binding energy of the lowest lying exciton in the C K absorption edge of nT. Shown is the range from smallest to largest binding energy for the inequivalent atoms of the different types of carbon atoms. The splitting of the respective excitonic state is given in brackets. All properties are in units of eV.

C type	α -C		β -C	
	min	max	min	max
2T	3.0 [0.15]	3.1 [0.14]	2.7 [0.13]	2.8 [0.13]
4T	2.3 [0.06]	2.3 [0.06]	2.0 [0.06]	2.1 [0.06]
6T	2.0 [0.05]	2.1 [0.05]	1.7 [0.05]	1.9 [0.05]

We can further compare the binding energies of the lowest lying excitons for all inequivalent C atoms. Our results are summarized in Tab. VI.1. We find that binding energies from transitions from the α -C atoms are larger than from the β -C atoms due to the higher electronegativity of S compared to C. With increasing n, the exciton binding energies and splitting of the lowest excitonic states are decreasing for both C types. The same trend has been observed for the band gap of nT, which depends almost linearly on the inverse of n [71], and the optical excitations of crystalline nT [65]. We attribute this effect to reduction of the average Coulomb interaction with increasing n: The excitons corresponding to π^* resonances are increasingly delocalized along the molecular chain which enhances dielectric screening, and thus results in the reduction of their binding energies. We want to note that the e-h wavefunction is delocalized only along the molecular chain and no charge transfer to adjacent molecules occurs for the lowest lying exciton pair for all investigated systems. This is in contrast to optical excitations where charge transfer excitons can be found for long-chain molecular crystals such as pentacene [46].

In summary, the attractive electron-hole interaction rules the formation of bound excitons in XAS while LFE play a minor role. Spectral features of the C K absorption edge can be attributed to transitions from two types of C atoms exhibiting or not exhibiting a covalent bond to a S atom. We have shown that our calculation for the bulk crystal replicates the experimental spectrum for 2T multilayers [17] which highlights the predominant molecular-like character of the spectral features. The π^* resonances are blueshifted up to 0.3 eV with increasing n. Binding energies of the lowest lying excitons are decreasing by up to 1 eV with increasing oligomer length. We attribute these results to the reduction of the average Coulomb interaction with increasing n, due to two effects: (1) delocalization of the e-h pair and (2) enhanced dielectric screening.

2 Sulfur K Absorption Edge

The S K absorption edge is commonly investigated to study the chemical composition of sulfur-containing fossil fuels. In this context, monothiophene [18, 72, 73], substituted thiophenes [74], and aromatic thiophenic compounds [73, 75] have been previously studied. To the best of our knowledge, results for oligothiophenes with longer chain oligomers are still missing. In this section, we explore the dependence of the S K absorption edge of nT crystals on the increasing oligomer length. We determine the origin of the spectral features as well as the difference of chemically inequivalent S atoms in 4T and 6T.

2.1 Analysis of XAS of Crystalline 4T

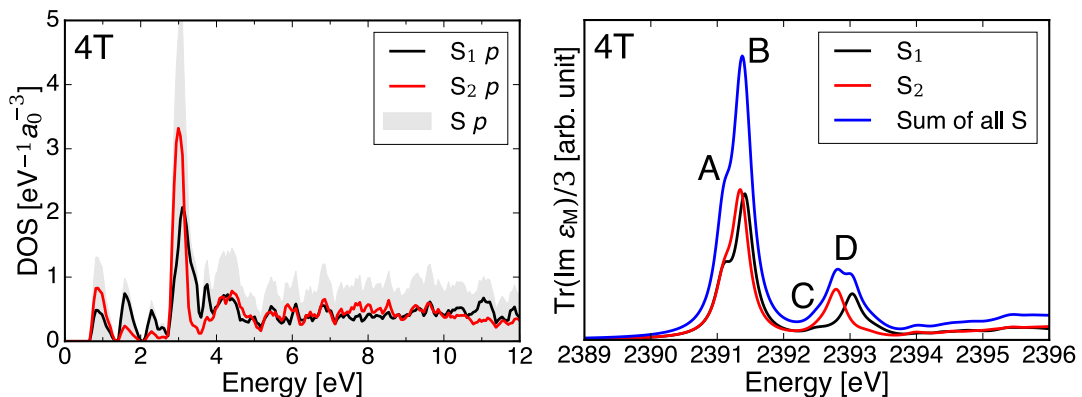


Figure 6.7: Left: Projected density of states of the S p states of 4T. The grey area represents the sum of all inequivalent S p contributions. Energies are relative to the Fermi level (set to zero in the mid-gap). Right: Absorption spectra from the S K edge of 4T. Shown is the solution of the BSE for the inequivalent S atoms as the average over the diagonal crystalline components of the imaginary part of the macroscopic dielectric tensor. The blue line denotes the contributions from all inequivalent S atoms.

Since there are no experimental references for oligothiophene crystals except monothiophene, we will focus on 4T crystals where only 2 inequivalent S atoms contribute to the XAS. We start our analysis of the S K absorption edge by comparing the solutions from the IPA and BSE for the inequivalent S_1 and S_2 atoms of 4T. The corresponding spectra are shown in Fig. 6.7 and Fig. 6.8 as the average of the diagonal crystalline components of the macroscopic dielectric tensor².

Analogous to the C K absorption edge, we can directly relate the S p PDOS of the conduction states in Fig. 6.7 to the corresponding IPA spectrum. Its features are reflected by the PDOS: The IPA spectrum is dominated by an intense peak B' which corresponds to the peak at 3.0 eV in the PDOS. It is formed by transitions to bands with σ^* character associated with the single S-C bond. At the IP onset, we find peaks with low intensity. They correspond to transitions to the LUMO+n subbands with π^* character. In this range, S_2 contributes more heavily to the LUMO

²The difference between Cartesian and crystalline components is illustrated in Appendix A.

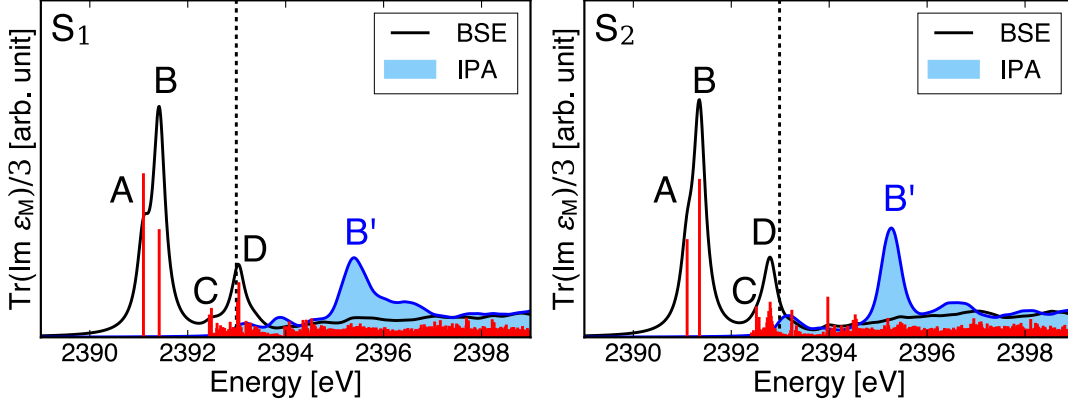


Figure 6.8: Absorption spectra from the inequivalent S K absorption edges of 4T. Shown is the average over the diagonal crystalline components of the imaginary part of the macroscopic dielectric tensor. Excitation energies (red vertical bars) and their oscillator strength are indicated by the height of the bars. Solutions from the BSE and the independent particle approximation (IPA) are shown in black and blue, respectively. The dashed line represents the independent particle onset.

subbands, whereas S_1 contributes equally to all LUMO+n subbands. This result is as expected since the LUMO is less localized on the S atom at the edge of the molecule (see Appendix B). At energies above 2397 eV, the IPA spectrum does not exhibit any pronounced peaks. This is reflected in the PDOS: It oscillates around a value of $0.5 \text{ eV}^{-1} a_0^{-3}$ for energies higher than 5.0 eV.

The inclusion of the electron-hole interaction in the BSE redshifts the spectrum by 1.9 eV and redistributes the oscillator strength to a few excitons. For the deep S K absorption edge, LFE play a minuscule role and induce no noticeable shift of the excitation energies (see Appendix B). The two inequivalent S atoms in 4T, with the $1s$ levels separated by 6 meV in the KS spectrum, contribute to the total absorption spectrum in Fig. 6.7. The BSE spectrum is dominated by two peak structures. Our labeling is indicated in Fig. 6.7 and Fig. 6.8. Peaks A and B are dominated by an exciton with large oscillator strength, whereas peaks C and D are formed by several transitions with non-vanishing oscillator strength. The lower-lying peak A has about half the intensity of peak B, and we find that both peaks are separated by 0.3 eV. We obtain the binding energies of the two most intense peaks, A and B, as the difference to their IPA counterparts, i.e., the IP onset for peak A and peak B' for B. The exciton corresponding to peak A has a binding energy of 1.90 eV for S_1 and 1.89 eV for S_2 . These values are comparable to the binding energies found for the C K absorption edge of 4T in Sec 1.2. For peak B, we obtain binding energies of 3.98 eV and 3.93 eV for S_1 and S_2 , respectively. They are, remarkably, more than twice as large than for the exciton of peak A. We attribute this difference to the underlying orbital character of the transitions and the aforementioned delocalization of the e-h wavefunction: Peak A is formed by transitions to π^* orbitals that are delocalized along the oligomer chain. The significant delocalization of the e-h pair of peak A and increased dielectric screening then reduces the average Coulomb interaction. In the case of peak B, transitions to σ^* orbitals occur. Here, the excitons are strongly localized on the respective S atom. As a result, the exciton binding

energy of peak A is reduced compared to peak B. The splittings of the excitonic state corresponding to peak A and B are 1 meV and 3 meV, respectively. They are a magnitude smaller than our reported splitting in the C K absorption edge of about 60 meV. These results indicate the highly localized character of the e-h pair and the minuscule role of intermolecular interactions for the deep S K absorption edge.

The most pronounced differences between the two inequivalent S atoms can be found in the peaks C and D. They are formed by several transitions with primarily π^* character, although they also exhibit mixing with σ^* states. For both inequivalent S atoms we find that peak C has very low intensity while peak D is more pronounced. While the energy position of peak C is only shifted by 30 meV between transitions from S₁ and S₂, peak D is redshifted by 250 meV. As a result, peak C appears as a shoulder of peak D in the spectrum from S₂.

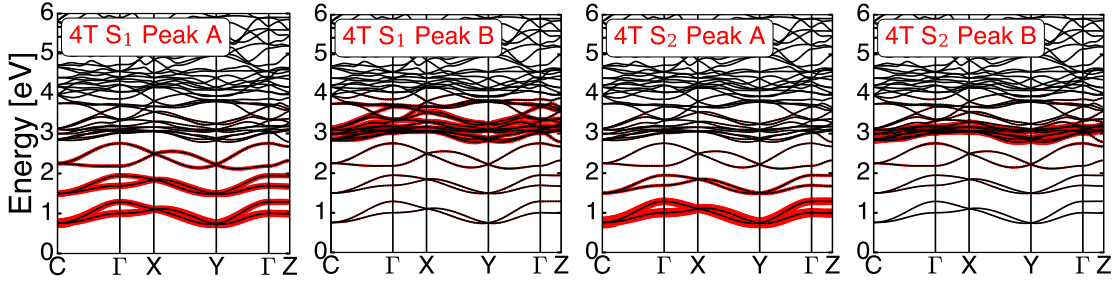


Figure 6.9: Excitonic weights of peak A and B of the S₁ and S₂ K absorption edge in crystalline 4T plotted on top of the Kohn-Sham band structure. The size of the red circles represents their magnitude. Energies are relative to the Fermi level (set to zero in the mid-gap).

For a quantitative comparison of the excitonic character of peaks A and B, we display in Fig. 6.9 the corresponding weights (see Eq. 3.54) plotted on top of the KS band structure. Peak A of S₁ is formed by transitions to the LUMO, LUMO+1, and LUMO+2 subbands with π^* character. For S₂, peak A is dominated by transitions to the LUMO subbands. Peak B is formed by transitions to the bands associated with the S-C single bond with σ^* character. The range of involved bands spans from 2.7 eV to 4.0 eV for S₁ and from 2.7 eV to 3.3 eV for S₂. We find that the underlying character of peaks A and B coincides in the spectra from the inequivalent S atoms. What changes, however, is the number of participating energy bands in the transitions which is determined by the corresponding S p PDOS displayed in Fig. 6.7. The homogenous distribution of the excitonic weights in reciprocal space reflects the localized intramolecular character of the e-h wavefunction in real space.

To further complement this quantitative analysis of the excitons, we visualize in Fig 6.10 the distribution of the e-h wavefunction in real space for a fixed hole position (see Eq. 3.52). The exciton wavefunction corresponding to peak A clearly resembles the character of a π^* orbital, being delocalized along the molecular chain, while peak B assumes the character of the final σ^* orbitals, being localized on the respective S atom and corresponding thiophene ring. Moreover, we find that the

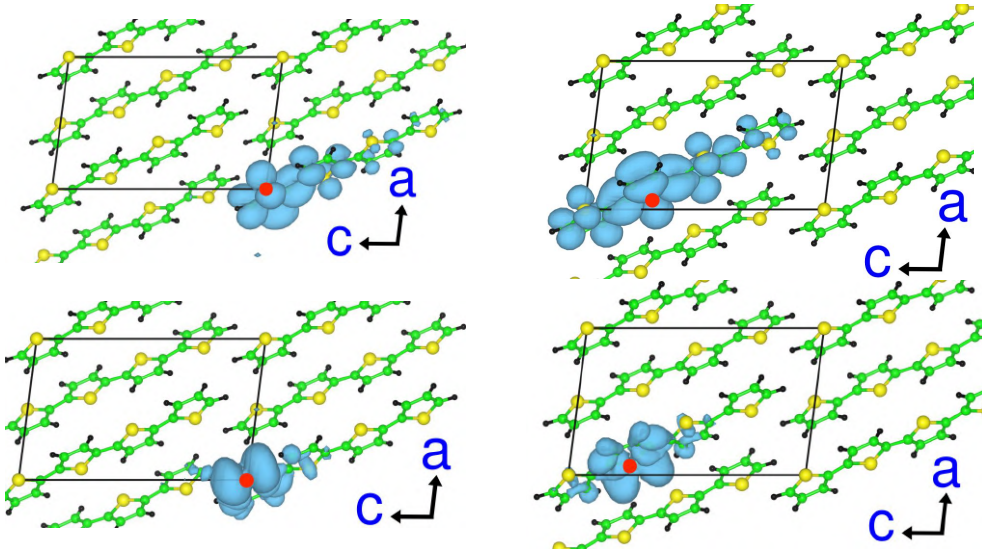


Figure 6.10: Real-space representation of the electron distribution of the exciton corresponding to peak A (top pictures) and B (bottom pictures) for the S₁ and S₂ *K* absorption edge in crystalline 4T. The hole is fixed near the probed atom and is marked by the red dot. The unit cell is indicated by the rectangle.

exciton wavefunction of both peaks is more delocalized when probing transitions from the atom in the inner thiophene ring, S₂. This, in turn, leads to the smaller exciton binding energies for excitations from S₂ compared to S₁. For both peaks, the e-h pair is confined on the respective 4T molecule and its wavefunction is not localized on adjacent oligomers. Our results for the S *K* absorption edge indicate that the distribution of the lowest-lying excitons in real space is solely intramolecular, determined by the covalent bonds within the oligomers.

2.2 Dependence on the Oligomer length

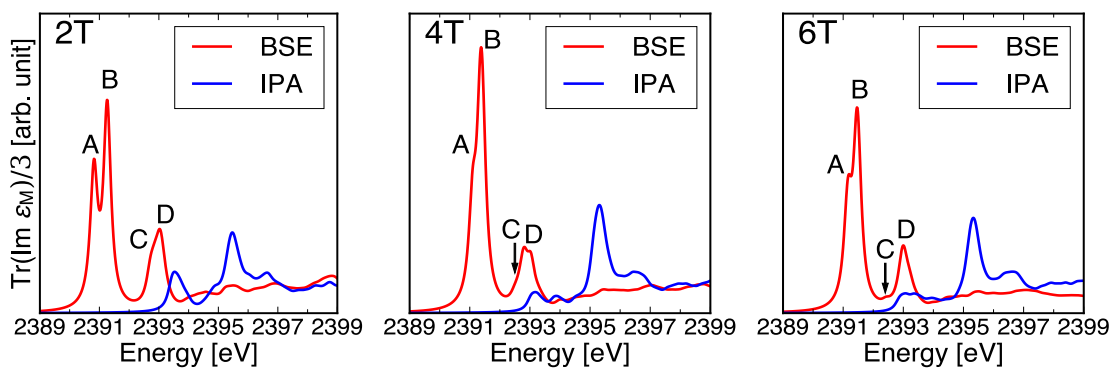


Figure 6.11: Absorption spectra from the S *K* absorption edge of crystalline nT from all inequivalent S atoms. The red and blue lines denote the solution of the BSE and the independent particle approximation, respectively. Shown is the average over the diagonal crystalline components of the imaginary part of the macroscopic dielectric tensor.

The BSE and IPA absorption spectra from all inequivalent S *K* absorption edges of nT are shown in Fig. 6.11. The overall spectral shape and intensity of the peaks are

very similar for all investigated systems. Peak B, however, is slightly enhanced in 4T compared to the other systems.

The main differences in spectral shape occur for the two lowest lying peaks in the BSE spectrum. The first peak, A, is blueshifted with increasing oligomer length n . Similar to the C K absorption edge, this effect is stronger when going from 2T to 4T than from 4T to 6T: Peak A of 2T is higher in energy by 0.28 eV in 4T and 0.31 eV in 6T. Peak B of 2T, on the other hand, is only higher in energy by 0.07 eV in 4T and 0.15 eV in 6T. The effect is therefore most pronounced for the π^* resonances while the σ^* resonances experience almost no shift. Similar results were found for α -substituted thiophenes where the π^* resonances vary substantially compared to the σ^* resonances for different ring substituents [74]. Analogous to the explanation for the C K absorption edge, we attribute this blueshift to the reduction of the average Coulomb interaction with increasing n . Peaks A and B are split by 0.5 eV in 2T, 0.3 eV in 4T, and 0.3 eV in 6T. For comparison, published experimental results report values of 0.5 eV for thiophene multilayers [76] and 0.7 eV for thiophene in solution [74]. We would estimate a splitting larger than 0.5 eV for monothiophene crystals according to the aforementioned blueshift with increasing n .

In Fig. 6.12, we distinguish the contributions from inequivalent S atoms in all investigated systems. Peaks A and B are nearly identical for transitions from all S atoms. The splitting of both peaks between the inequivalent S atoms is less than 60 meV. i.e., on the order of the core level shift of S $1s$ (33 meV) in 6T. We attribute the small difference between S atoms to the different chemical character of the respective C bonding partners. Remarkably, peak D from S_1 is blueshifted by 0.2-0.3 eV with respect to its counterpart from the other S atoms in 4T and 6T. This result is somewhat surprising since we would expect a small redshift of π^* resonances of S_1 , due to the decreased correlation effects for the S atom at the edge of the molecule. Convergence issues could be one possible explanation. This, however, seems rather unlikely, since this feature is present for both 4T and 6T for which separate convergence tests were performed. Another possible explanation is the different contributions to the electronic structure from both S atoms. This will be further explained in the following section which presents the S $L_{2,3}$ absorption edge. As far as we know, this blueshift of peak D for S_1 has not been reported previously since most studies concentrate on thiophenic

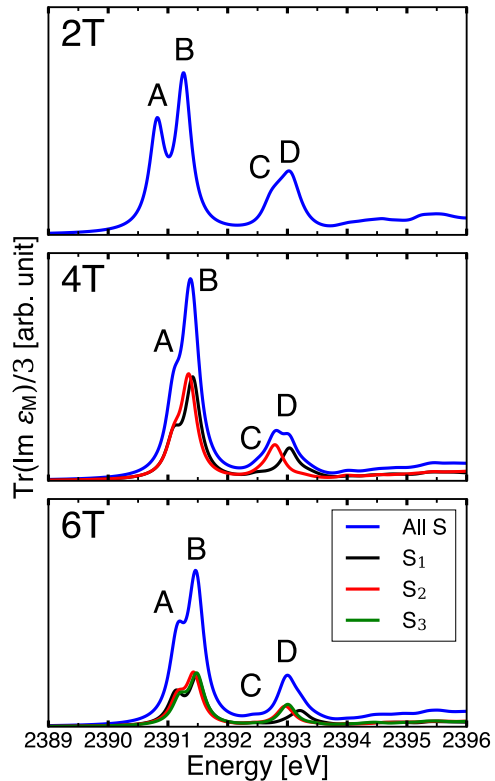


Figure 6.12: Absorption spectra from the S K absorption edge of crystalline nT with the contribution from all inequivalent S atoms in blue.

crystalline nT with the contribution from all inequivalent S atoms in blue.

compounds with one S atom [73–76].

To summarize, we find four main spectral features in the S K absorption edge of nT crystals: (1) The first peak A is formed by transitions to the subbands with π^* character associated with the LUMO orbital in the thiophene molecule. (2) Peak B is most intense and is formed by transitions to the subbands with σ^* character associated with the S-C bond. (3) The weakest resonance C has mixed π^* and σ^* character. (4) The peak D is also formed by multiple transitions to bands with hybridized π^* and σ^* character. Our assignment of peaks A and B coincides with experimental results for thiophene multilayers [76] and molecular thiophene [18, 72, 74]. Hitchcock *et al.* have assigned peaks C and D to transitions to higher lying σ^* orbitals [18]. Our results indicate that they are actually formed by transitions with mixed π^* and σ^* character.

Table VI.2: Binding energies of the two most intense excitons, A and B, in the S K absorption edge of crystalline nT. Values are obtained as the difference in the excitation energy to their respective IPA counterpart, i.e, IP onset for A and B' for B. All energies are in units of eV.

Peak	A			B		
	S ₁	S ₂	S ₃	S ₁	S ₂	S ₃
2T	2.6			4.2		
4T	1.9	1.9		4.0	3.9	
6T	1.7	1.7	1.6	3.9	3.9	3.8

Lastly, we compare the binding energies of the excitons corresponding to peaks A and B for the investigated systems (in Tab. VI.2). Analogous to our results for the C K absorption edge, the exciton binding energy of peak A is reduced by about 1 eV when going from 2T to 6T. Additionally, we find smaller values for the spectra from S atoms in the inner thiophene rings ($S_1 > S_2 > S_3$). We attribute this result to the reduction of the average Coulomb interaction with increasing oligomer length. The exciton binding energies of peak B are also slightly reduced with increasing n , with the reduction in 6T being of 0.4 eV. The smaller decrease compared to peak A originates from the underlying character of the transition: σ^* resonances are less affected by the increased aromatic character of longer oligomers and remain largely localized on the probed atom and on the respective monomer (see also Fig. 6.10).

3 Sulfur $L_{2,3}$ Absorption Edge

The S $L_{2,3}$ absorption edge has been studied experimentally for different oligothiophene films such as monothiophene [17–19], bithiophene [17, 21, 22], and polythiophene films [77]. The main goal was to identify the formation of chemisorptive bonds with a substrate and it previously revealed the cleavage of the C-S bond of monothiophene films on Pt(111) [19]. The assignment of the spectral features, however, appears rather controversial in the literature [17, 18, 21, 22]. First principles studies of core spectra commonly supplementing experimental results are performed in the half core hole approximation. While this approach is known to be accurate for K absorption edges, spin-orbit coupling effects are neglected, and thus $L_{2,3}$ absorption edges can hardly be reproduced. The approach employed in this work, however, enables us to accurately treat spin-orbit coupling. Our results match very well the experimental splitting of 1.3 eV in the S $2p$ levels of thiophene [78, 79]. In this section, we present an accurate calculation of the S $L_{2,3}$ absorption edge for oligothiophene crystals. We provide a comprehensive assignment of the spectral features and an in-depth analysis of their origin in terms of electronic contributions. Finally, we investigate the dependence of exciton binding energies and the spectra with respect to the oligomer length.

3.1 Analysis of XAS of Crystalline 2T

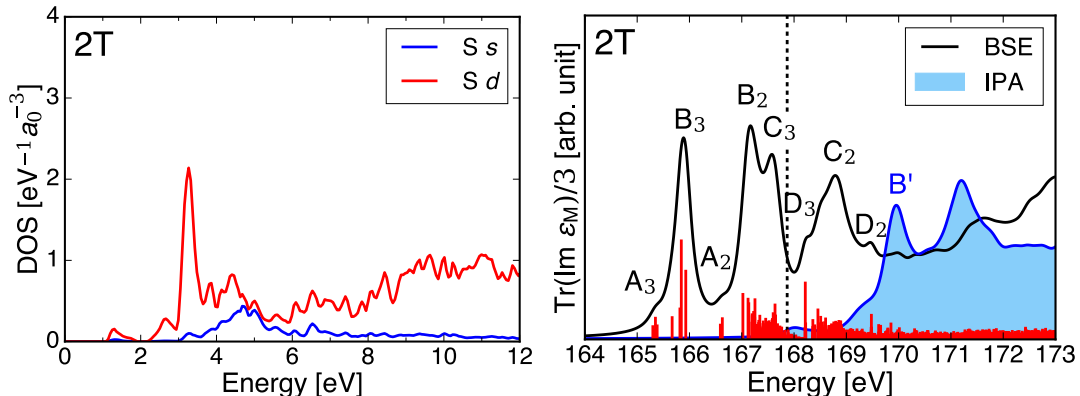


Figure 6.13: Left: Projected density of states of the S s and S d states of 2T. Energies are relative to the Fermi level (set to zero in the mid-gap). Right: Absorption spectra from the S $L_{2,3}$ absorption edge of 2T averaged over the diagonal Cartesian components. Excitation energies and their oscillator strength indicated by the height of the vertical bars, as obtained from a BSE calculation. Spectra from the BSE and the independent particle approximation are shown in black and blue, respectively. The dashed line represents the independent particle onset.

In Fig. 6.13, the S $L_{2,3}$ absorption edge of 2T obtained from the BSE and the IPA is shown. Since dipole-allowed transitions occur only from the initial core p states to conduction states with s or d character, we start our analysis by comparing the S s and d PDOS of 2T on the left side of Fig. 6.13 with the IPA absorption spectrum. The IPA spectrum reflects the features in the PDOS: The two intense peaks at 170.1 eV and 171.3 eV correspond to the peaks at 3.0 eV and 5.0 eV in the PDOS, respectively. The first peak is formed by transitions to bands associated with the

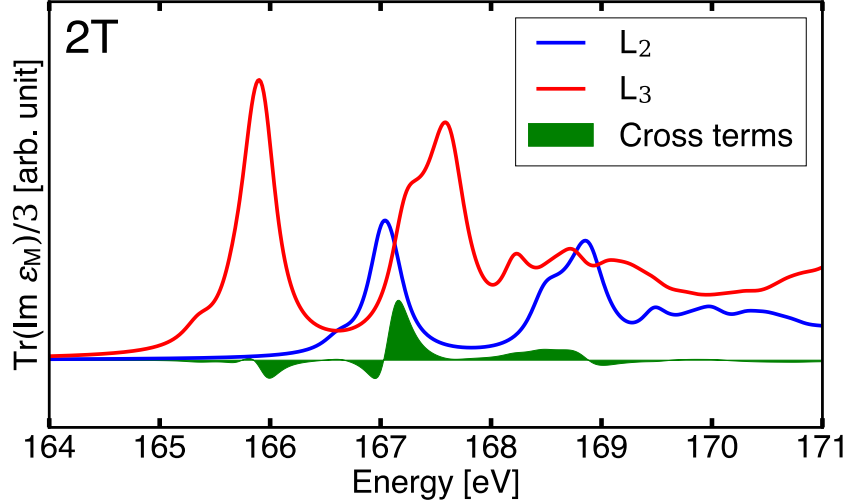


Figure 6.14: Separation of the S $L_{2,3}$ absorption spectrum in L_2 , L_3 , and cross term contributions. A Lorentzian broadening of 150 meV is applied.

S-C bond, while the second peak is formed by transitions to bands with hybridized S s and d character. At the IP onset, we find a peak with low intensity. It is formed by transitions to the LUMO subbands which exhibit small contributions from the S d states. In the high-energy part of the IPA spectrum the oscillator strength is non-vanishing. This reflects the PDOS after 6.0 eV where it is dominated by increasing contributions from S d states.

As seen on the right side of Fig. 6.13, in the solution of the BSE the spectrum is redshifted by 3 eV compared to the IPA spectrum and the oscillator strength is redistributed to a few excitons. LFE, however, play no significant role in the formation of excitons and shift the excitation energies by less than 150 meV (see Appendix B).

We can identify several features that originate from the L_2 and L_3 absorption edges, as well as by their mixing. The approach employed in this work enables us to separately calculate the contributions from different initial core states. We display the full $L_{2,3}$ absorption spectrum as well as its subedges in Fig. 6.14. Here, L_2 (L_3) denotes contributions from the $2p_{1/2}$ ($2p_{3/2}$) states alone, and cross terms represent the difference between the total $L_{2,3}$ spectrum and the sum of the L_2 and L_3 spectra. The L_2 spectrum is, as expected, blueshifted by 1.3 eV compared to the L_3 spectrum due to spin-orbit coupling. In the independent particle picture, we obtain a branching ratio of 2 : 1 for the L_3 and L_2 subedges, which reflects the ratio between the number of M_J -states. The cross terms significantly lower the branching ratio by transferring intensity from the L_3 to the L_2 edge. This effect is most pronounced from 167.0 eV to 167.5 eV where significant mixing of both subedges occurs. Similar results have been found for the $L_{2,3}$ absorption edge of $3d$ transition elements, e.g., in TiO_2 where the branching ratio is reduced to approximately 1 : 1 [11].

Table VI.3: Excitation energies (E) of the spectral features in the S $L_{2,3}$ absorption edge of crystalline 2T. Exciton binding energies E_b are obtained as the difference in excitation energy with respect to their IPA counterparts, i.e., the IP onset for π^* (LUMO) and peak B' for σ^* (S-C) resonances.

Peak	E [eV]	E_b [eV]	Assignment
A ₃	165.3-165.4	2.6	$2p_{3/2} \rightarrow \pi^*$ (LUMO,LUMO+1)
B ₃	165.7-165.9	4.3	$2p_{3/2} \rightarrow \sigma^*$ (S-C)
A ₂	166.6	1.3	$2p_{1/2} \rightarrow \pi^*$ (LUMO,LUMO+1)
B ₂	167.0-167.1	3.0	$2p_{1/2} \rightarrow \sigma^*$ (S-C)
C ₃	167.3-167.6	0.6	$2p_{3/2} \rightarrow \pi^*$ (LUMO)
			$2p_{3/2} \rightarrow \pi^*$ (LUMO)
			$2p_{1/2} \rightarrow \sigma^*$ (S-C)
D ₃	168.2		$2p_{3/2} \rightarrow$ mixed σ^* , π^* (LUMO+1)
C ₂	168.5-168.9		$2p_{1/2} \rightarrow \pi^*$ (LUMO)
D ₂	169.5		$2p_{1/2} \rightarrow$ mixed σ^* , π^* (LUMO+1)

We now further analyze the BSE spectrum from the S $L_{2,3}$ absorption edge of crystalline 2T. To guide the reader, we label the spectral features in Fig. 6.13. Here, the subscripts, 2 and 3, denote if the feature originally stems from the L_2 or L_3 edge. An enumeration of all spectral features and corresponding binding energies is given in Tab. VI.3. The $L_{2,3}$ spectrum is dominated by three peak structures with comparable intensity: (1) peak B₃, (2) the peak structure formed by peaks B₂ and C₃, and (3) peak C₂. First, we analyze the features originating from the L_3 absorption edge, i.e., the S $2p_{3/2}$ states. The shoulder A₃ is formed by four excitons with low oscillator strength, and corresponds to transitions to the LUMO and LUMO+1 subbands with π^* character. The intensity of this feature is very small due to the predominant p character of the LUMO subbands (see Fig. 5.2). For the lowest lying exciton, we calculate a binding energy of 2.6 eV and a splitting of 44 meV. It is delocalized along the molecular chain but confined on the respective 2T molecule. Analogous to the lowest lying excitons in the C K and S K absorption edges, the e-h wavefunction is not localized on adjacent molecules. The second peak, B₃, is solely formed by transitions to the σ^* orbitals associated with the S-C bond. It is dominated by 4 excitons with large oscillator strength. They are highly localized on the respective S atom and 2T molecule, evident by the larger binding energy of 4.3 eV compared to A₃. The splitting of the lowest lying excitons of peak B₃ is 150 meV. Remarkably, the binding energies of peaks A₃ and B₃ are almost equal to the ones obtained for the two intense peaks, A and B , in the S K absorption edge of 2T. The exciton splittings, however, are considerably larger for the S $L_{2,3}$ absorption edge and are comparable to the results found for the C K absorption edge, where the splitting ranges from 130 meV to 150 meV. This results from the comparable energies of the C $1s$ and S $2p$ core states.

Several excitons contribute to the third peak C₃. It is predominately formed by transitions with π^* character to the LUMO subbands. The overlap with peak B₂ leads to an additional mixing with transitions from the S $2p_{1/2}$ to the σ^* states,

but this does not significantly alter its excitonic character. Lastly, we can identify the shoulder D_3 at 168.2 eV which is dominated by an exciton with large oscillator strength. It is formed by transitions with mixed π^* and σ^* character to the LUMO+1 subbands and higher bands up to 5.0 eV. As shown in the PDOS in Fig. 6.13, these higher lying states are of mixed S s and d character. A quantitative comparison of the excitonic character of all peaks is given in Appendix B. For the L_2 absorption edge, the spectral features are blueshifted by 1.3 eV due to the spin-orbit coupling, but the corresponding transitions occur to the same conduction states as in the L_3 edge. Peak B_2 also results from significant mixing between transitions from the S $2p_{3/2}$ states to the LUMO subbands and transitions from the S $2p_{1/2}$ states to bands with σ^* character.

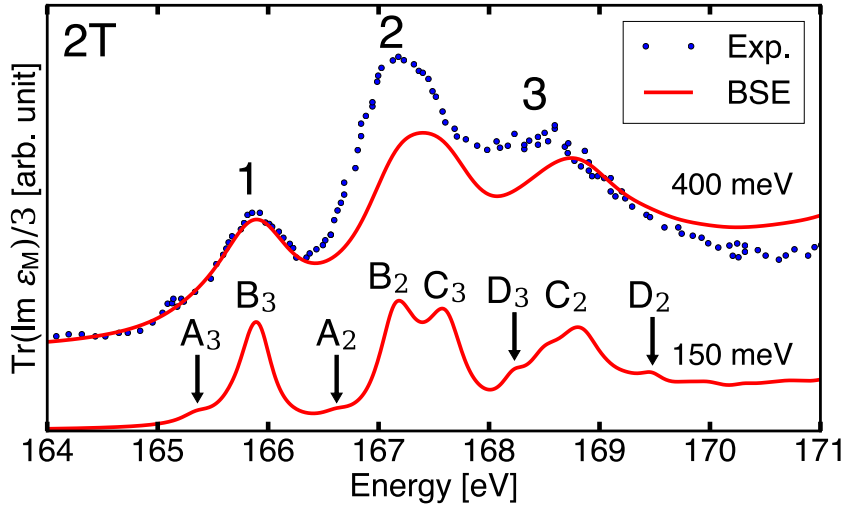


Figure 6.15: S $L_{2,3}$ absorption spectrum of 2T averaged over the diagonal Cartesian components. The solution of the BSE is shown in red and experimental data taken from [17] is shown in blue. A Lorentzian broadening of 400 meV is applied (top curve). A smaller broadening of 150 meV is applied to resolve all spectral features (bottom curve).

In Fig. 6.15, we compare our results with the experimental spectrum obtained for 2T multilayers on Ag(111) [17]. The calculated spectrum is shifted by 15.3 eV to align it at the first absorption peak with the measured one. We apply a Lorentzian broadening of 400 meV to reproduce the experimental spectrum. Since no information on the setup of the measurements is available, we compute the spectrum as the average over the diagonal Cartesian components of the macroscopic dielectric tensor. The three intense resonances found in the experimental spectrum, (1), (2), and (3), are well replicated by our calculation. With such a broadening, we are not able to resolve less intense features that are experimentally observed, e.g. the A_3 shoulder at 165.3 eV. It is, however, well known that each peak in the $L_{2,3}$ XAS has its own broadening [80]. For an even more quantitative agreement with experiment, we would therefore need to apply an energy-dependent broadening. Nonetheless, a smaller broadening of 150 meV is sufficient to resolve the less intense features. In excellent agreement with our results (see Tab. VI.3), all previous studies assign

resonance (1) to transitions from S $2p_{3/2}$ states to σ^* orbitals associated with the S-C bond [17, 18, 21, 22]. Väterlein *et al.* [17] assign the second resonance (2) to a superposition of S $2p_{1/2} \rightarrow \sigma^*$ (S-C) transitions and Rydberg-like transitions from the S $2p_{3/2}$ states to higher energy σ^* orbitals, which actually is in disagreement with our results,. They assign the third resonance (3) to Rydberg-like transitions from S $2p_{1/2}$ states to higher energy σ^* orbitals. We, on the other hand, assign the second resonance (2) to the superposition of S $2p_{1/2} \rightarrow \sigma^*$ (S-C) transitions and S $2p_{3/2} \rightarrow \pi^*$ (LUMO) transitions. The splitting between the two peaks contributing to the second resonance (2), B₂ and C₃, is 0.4 eV. This is in good agreement with the experimental value of 0.4 eV [22]. Consequently, the third resonance (3), i.e. peak C₂, is formed by S $2p_{1/2} \rightarrow \pi^*$ (LUMO) transitions. Our assignment is in agreement with other published experimental results [18, 21, 22]. Some effort has also been made to correctly describe the less intense features in the S $L_{2,3}$ spectrum commonly observed in experimental results [17, 18, 22]. Our results, however, are the first comprehensive assignment of all spectral features using many-body theory: We attribute the weak shoulder A₃ at 165.3 eV to S $2p_{3/2} \rightarrow \pi^*$ (LUMO, LUMO+1) transitions. This peak is resolved in multiple experiments [17, 22]. Peak A₂ at 166.6 eV, however, has not been resolved. Additionally, Koller *et al.* [22] found that the third resonance (3) is straddled by two weaker resonances which they assign to transitions from the S $2p$ states to the LUMO+1 subbands. Our calculation matches very well this result: We find two weaker resonances, D₃ and D₂, that straddle the intense resonance C₂. Here, peaks D₃ and D₂ are formed by transitions with mixed π^* and σ^* character from the S $2p_{1/2}$ and S $2p_{3/2}$ states to the LUMO+1 subbands and higher bands up to 5.0 eV (see also the PDOS in Fig. 6.13).

3.2 Dependence on the Oligomer Length

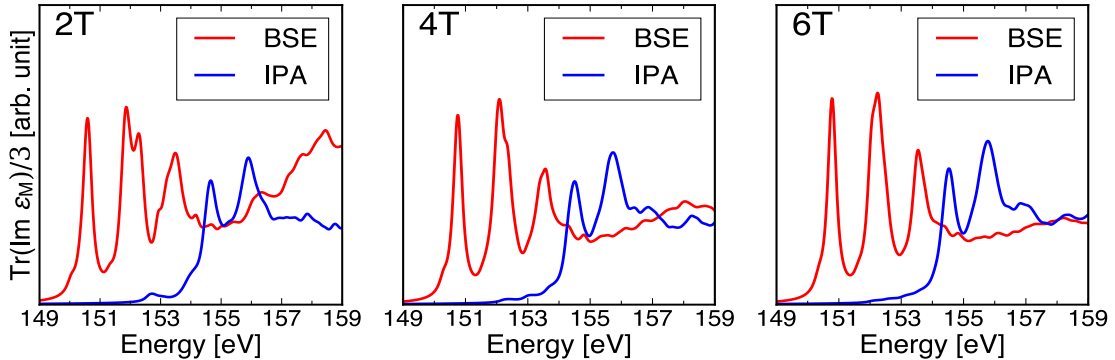


Figure 6.16: Absorption spectra from the S $L_{2,3}$ absorption edge of crystalline nT from all inequivalent S atoms. The red and blue lines denote the solution of the BSE and the independent particle approximation, respectively. Shown is the average over the diagonal Cartesian components of the imaginary part of the dielectric tensor.

We now want to identify similarities and differences in the XAS at increasing oligomer length. The BSE and IPA absorption spectra from the S $L_{2,3}$ edge for all inequivalent S atoms are shown in Fig. 6.16. We obtain a splitting of 1.3 eV between peaks A₃ (B₃) and A₂ (B₂), which is reduced to 1.2 eV in 4T and 6T. The overall spectral shape as well as the intensity of the peaks are very similar for all

investigated systems. In the high-energy part of the BSE spectrum of 2T the oscillator strength increases above 155 eV. This does not occur in the absorption spectra of 4T and 6T, due to the smaller number of higher lying conduction states included in the corresponding calculations (see Chapter IV).

A noticeable difference in the spectra of 2T to 6T is the blueshift of the two lowest lying peaks, A_3 and B_3 , as well as peaks A_2 and B_2 with increasing oligomer length n . Analogous to our previous results for the lowest lying peaks in the C K and S K absorption edge, we find that this shift is larger when going from 2T to 4T than from 4T to 6T. Remarkably, it is almost rigid for these resonances: The first peak, A_3 , of 2T is shifted by 0.22 eV in 4T and 0.29 eV in 6T. The more intense second peak of 2T, B_3 , is shifted by 0.22 eV in 4T and by 0.25 eV in 6T. This is in contrast to our results for the C K and S K absorption edges where we found a more pronounced shift for the π^* resonances compared to the σ^* resonances. This blueshift is nearly identical to the one calculated for peak A of the S K absorption edge. We therefore attribute this effect to the delocalization of the e-h pair with increasing n .

The most pronounced difference in the spectra for the three oligomers appears for the second resonance (2) in the range from 151.5 eV to 153.0 eV. The energy difference between the two peaks contributing to this resonance, B_2 and C_3 , is decreasing with increasing oligomer length n : Both peaks are separated by 0.4 eV in 2T while by 0.3 eV and 0.2 eV in 4T and 6T, respectively. This is the result of the aforementioned blueshift of peak B_2 as well as of the individual contributions from the inequivalent S atoms: We find that the separation of the peaks B_2 and C_3 is only decreasing for the S atoms in the inner thiophene rings, S_2 and S_3 . This effect is illustrated on the left side of Fig. 6.17, where we distinguish the contributions from the inequivalent S atoms in all investigated systems.

Similar to the S K absorption edge, the two lowest lying peaks, A_3 and B_3 , are nearly identical in the spectra from all S atoms. The splitting of both peaks between the spectra from inequivalent S atoms is less than 70 meV, which is one order of magnitude larger than the core-level shift of S $2p$ states of 3 meV in 6T. We attribute this behaviour to the slightly different chemical character of their respective C bonding partners. The situation is different for the higher energy peaks, C_2 and C_3 : As shown on the right side of Fig. 6.17, these peaks are blueshifted by 0.3 eV for the spectra from the S atom in the outer thiophene ring, S_1 , compared to the spectra from the other S atoms. Remarkably, this value is similar to the blueshift of the high energy peak D in the S_1 K absorption spectrum ranging from 0.3 eV to 0.4 eV. We believe this shift originates from the different contributions of the S atoms to the electronic structure, since it occurs in both S absorption edges. Another supporting argument concerns the nature of the shifted resonances: Peaks C_2 and C_3 in 4T and 6T are mainly formed by transitions to the LUMO and LUMO+1 subbands with π^* character. These subbands are of S p character hybridized with S d states (see PDOS in Fig. 5.2). Dipole-allowed transitions from the S $2p$ states hit the S d contribution of the LUMO+ n bands. To prove this, we project for the inequivalent S atoms of 6T bands with S d character on top of the Kohn-Sham band structure in Fig. 6.18. We find that the LUMO subbands are mainly of S_2 and S_3 d character.

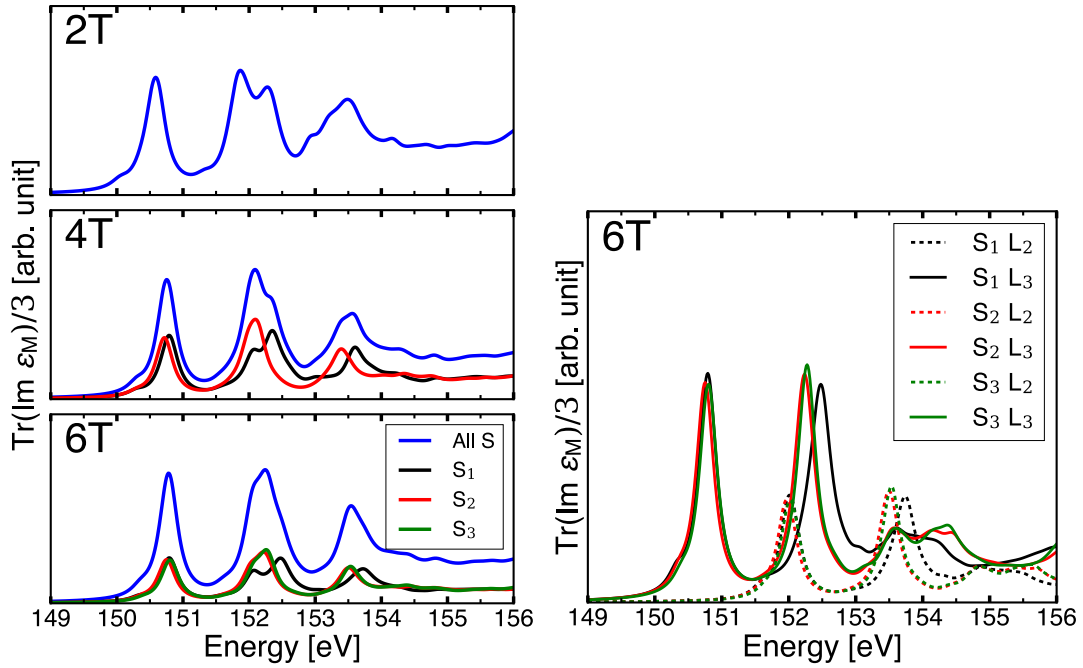


Figure 6.17: Left: Absorption spectra from the S $L_{2,3}$ absorption edge of crystalline nT with the contribution from all inequivalent S atoms in blue. Shown is the average over the diagonal Cartesian components. Right: Separation of the S $L_{2,3}$ absorption spectrum of crystalline 6T in the L_2 and L_3 contributions from all inequivalent S atoms.

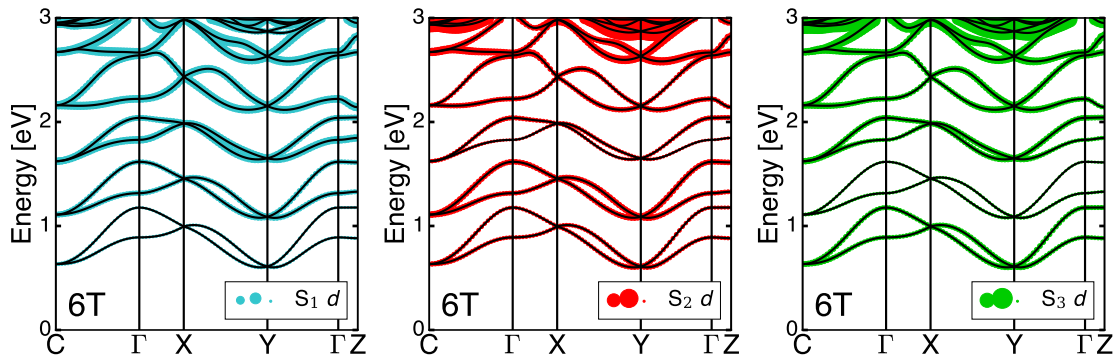


Figure 6.18: S d projected band character for the inequivalent S atoms in 6T. Energies are relative to the Fermi level, set to zero in the the mid-gap.

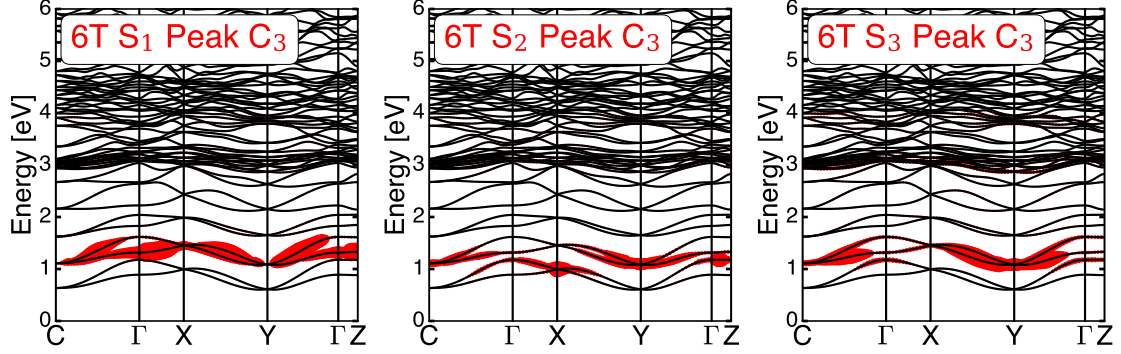


Figure 6.19: Excitonic weights of the most intense exciton contributing to the peak C_3 in the spectra from the S_1 , S_2 , and S_3 $L_{2,3}$ absorption edges in crystalline 6T, plotted on top of the Kohn-Sham band structure. The size of the red circles represents the magnitude of the weights. Energies are relative to the Fermi level (set to zero in the mid-gap).

For a quantitative comparison with the excitonic character of peak C_3 , we display in Fig. 6.19 the weight of the most intense exciton contributing to this peak. The excitonic character reflects the bandcharacter of the LUMO+n subbands: Peak C_3 from S_1 is solely formed by transitions to the LUMO+1 subbands, while it is given in the spectra from S_2 and S_3 by transitions to both the LUMO and LUMO+1 subbands. This leads to a blueshift of the corresponding resonance in the spectrum from S_1 compared to its counterpart in the spectra from the other S atoms. It is important to note that this shift only occurs for weakly bound excitons and not strongly bound excitons, such as those corresponding to peak A_3 (see Fig. 6.17).

Table VI.4: Binding energies of the lowest lying excitons contributing to the peaks A_3 and B_3 in the S $L_{2,3}$ absorption edge of crystalline nT. Values are obtained as the difference in the excitation energy to their respective IPA counterpart, i.e., IP onset for A and B' for B. All energies are in units of eV.

Peak	A_3			B_3		
	S_1	S_2	S_3	S_1	S_2	S_3
2T	2.6			4.3		
4T	1.9	1.9		3.9	3.8	
6T	1.7	1.7	1.6	3.9	3.9	3.8

Lastly, we compare the binding energies of the lowest lying excitons contributing to peaks A_3 and B_3 for all investigated systems (Tab. VI.4). The exciton binding energy of peak A_3 is reduced by about 1 eV when going from 2T to 6T. We attribute this result to reduction of the average Coulomb interaction with increasing oligomer length. Smaller values are found for the spectra from the S atoms in the inner thiophene rings ($S_1 > S_2 > S_3$). This is resulting from the e-h pair being more delocalized when probing transitions from the atoms in the inner thiophene rings.

The binding energies of the excitons corresponding to peak B_3 are only reduced by about 0.5 eV compared to peak A_3 . The smaller decrease compared to peak A_3 originates from the nature of the transitions: σ^* resonances are less affected by the increased aromatic character of longer oligomers and remain largely localized on the probed atom and on the respective monomer. Remarkably, these results are almost identical to the ones obtained for the lowest lying peaks, A and B, in the S K absorption edge (compare Tab. VI.2). We attribute this behaviour to the similar nature of the transitions: In both absorption edges, the lower lying peaks are formed by transitions to the same conduction bands: (1) the LUMO+n subbands and (2) the bands of σ^* character associated with the S-C bond at approximately 3 eV (see PDOS in Fig. 5.2). These bands of mainly C p and S p character are also hybridized with the S d states. This hybridization leads to the similar exciton properties for the S K and S $L_{2,3}$ absorption edges.

VII Summary and Outlook

In this work, we have calculated the electronic structure and core spectra of oligothiophene crystals nT (n=2,4,6), a well known family of semiconducting organic molecular crystals. All calculations were performed in the (L)APW+lo formalism using the all-electron full potential **exciting** code for DFT and MBPT calculations. X-ray absorption spectra were calculated from *ab-initio* MBPT through the solution of the BSE. Our investigation of the electronic structure was concentrated on the conduction states, since they are probed by X-ray absorption spectroscopy. The lower lying conduction bands are formed by π^* orbitals while the most intense peak in the density of states at 3 eV is formed by σ^* orbitals. The individual atomic contributions to the unoccupied states were used to analyze the obtained core spectra. Our results for the electronic band structure are in good agreement with previously published results.

We find that the attractive electron-hole interaction is the driving force behind core-level excitations in these systems. Exciton binding energies are on the order of eV. We obtain a singlet-triplet splitting which is one order of magnitude smaller than exciton binding energies; thus, local-field effects play a miniscule role. The overall spectral shape and intensity of the main peaks in all the absorption edges is very similar for all investigated systems. The exciton binding energies, however, are decreasing by up to 1.0 eV, going from 2T to 6T. This is resulting from a reduction of the average Coulomb interaction, due to (1) the increased delocalization of the e-h pairs with increasing oligomer length and (2) an increased effect of the dielectric screening. π^* resonances, which are delocalized along the molecular chain, are affected more strongly than σ^* resonances, which are localized on the respective atom.

In the carbon (C) *K* absorption edge, the spectral features can be assigned to transitions from two types of C atoms: C atoms with a covalent bond to S and C atoms without such a bond. The full BSE spectrum is dominated by three intense excitonic resonances: The first two resonances correspond to transitions from both C types to the LUMO subbands with π^* character. Going from 2T to 6T, we obtain binding energies of the lowest lying excitons ranging from 3.1 eV to 2.1 eV. The third resonance is formed by transitions to states with σ^* character associated with the S-C bond. Our results are in excellent agreement with published experimental results for 2T and 6T multilayers.

In the sulfur (S) *K* absorption edge, the contributions from inequivalent S atoms to the spectrum are nearly identical in all the systems. We observe two types of intense excitonic resonances. The first resonance is formed by transitions to the LUMO+n subbands with π^* character, while the second resonance is formed by transitions to bands with σ^* character. Going from 2T to 6T, we obtain exciton binding energies of 2.6 eV to 1.6 eV and 4.3 eV to 3.8 eV for the first and second resonance, respectively.

For the sulfur $L_{2,3}$ absorption edge, we find that the spectrum can not be separated into its subedges, due to the small spin-orbit coupling between the S $2p_{1/2}$ and S $2p_{3/2}$ states. It is dominated by three intense resonances: (1) The first resonance is formed by S $2p_{3/2} \rightarrow \sigma^*$ (S-C) transitions, (2) the second resonance results from significant mixing between S $2p_{1/2} \rightarrow \sigma^*$ (S-C) and S $2p_{3/2} \rightarrow \pi^*$ (LUMO) transi-

tions, and (3) the third resonance is formed by S $2p_{1/2} \rightarrow \pi^*$ (LUMO) transitions. For the excitons contributing to the two lowest lying peaks, we find binding energies of 2.6 eV to 1.6 eV and 4.3 eV to 3.8 eV, respectively. The contribution to the second and third resonance from the S atom at the edge of the oligomer is slightly different compared to the one from the other S atoms. This difference originates from the different contributions of these atoms to the LUMO+n subbands. Our approach accurately replicates experimental spectra for 2T multilayers.

This study provides a comprehensive description of core excitations in oligothiophene crystals. As such, our results are important in view of a complete characterization of the light-matter interaction in these materials. Our work further confirms the predictive power of many-body perturbation theory in determining the character of the excitonic resonances and their dependence on the oligomer length.

In the future, we aim to further investigate the effect of intermolecular interactions on the absorption edges. By comparing the calculated spectra for the crystalline and molecular form of oligothiophene, we can determine the dependence of the spectral features on the packing density. In conjunction with the present results, this can provide insight into the electronic properties of oligothiophene and polythiophene films. We also plan to collaborate with colleagues specialized in XAS, to compare our results for the exciton binding energies, and their dependence on the oligomer length, with experimental data. We believe that our calculated exciton binding energies underestimate the experimental values. The LDA functional, which is used in this work, is known to be inaccurate for molecular crystals [36], where a description of the intermolecular van der Waals interaction is important. As such, we aim to investigate the dependence of our results on the employed exchange-correlation functional.

Bibliography

- [1] Gilles Horowitz, Organic field-effect transistors. *Advanced Materials* **10** (5), (1998), 365–377.
- [2] M Granstrom, K Petritsch, A C Arias, A Lux, M R Andersson and R H Friend, Laminated fabrication of polymeric photovoltaic diodes. *Nature* **395** (6699), (1998), 257–260.
- [3] Stephen R Forrest, The path to ubiquitous and low-cost organic electronic appliances on plastic. *Nature* **428** (6986), (2004), 911–918.
- [4] Stephen R. Forrest, The road to high efficiency organic light emitting devices. *Organic Electronics* **4** (2), (2003), 45 – 48.
- [5] Igor F. Perepichka and Dmitrii F. Perepichka, eds., Handbook of Thiophene-Based Materials: Applications in Organic Electronics and Photonics. John Wiley & Sons, Ltd (2009).
- [6] Tian An Chen and Reuben D. Rieke, The first regioregular head-to-tail poly(3-hexylthiophene-2,5-diyl) and a regiorandom isopolymer: nickel versus palladium catalysis of 2(5)-bromo-5(2)-(bromozincio)-3-hexylthiophene polymerization. *Journal of the American Chemical Society* **114** (25), (1992), 10087–10088.
- [7] Tian An Chen, Richard A. O’Brien and Reuben D. Rieke, Use of highly reactive zinc leads to a new, facile synthesis for polyarylenes. *Macromolecules* **26** (13), (1993), 3462–3463.
- [8] Gilles Horowitz, Denis Fichou, Xuezhou Peng, Zhigang Xu and Francis Garnier, A field-effect transistor based on conjugated alpha-sexithienyl **72**, (1989), 381–384.
- [9] Joachim Stöhr, NEXAFS Spectroscopy. Springer-Verlag Berlin Heidelberg (1992).
- [10] Isao Tanaka and Teruyasu Mizoguchi, First-principles calculations of x-ray absorption near edge structure and energy loss near edge structure: present and future. *Journal of Physics: Condensed Matter* **21** (10), (2009), 104201.
- [11] Christian Vorwerk, Caterina Cocchi and Claudia Draxl, Addressing electron-hole correlation in core excitations of solids: An all-electron many-body approach from first principles. *Phys. Rev. B* **95**, (2017), 155121.
- [12] Claudia Draxl and Caterina Cocchi, Exciting core-level spectroscopy, arXiv preprint arXiv:1709.02288 (2017).
- [13] Robert Laskowski and Peter Blaha, Understanding the $L_{2,3}$ x-ray absorption spectra of early 3d transition elements. *Phys. Rev. B* **82**, (2010), 205104.
- [14] Christian Vorwerk, All-electron many-body approach to x-ray absorption spectroscopy. Master thesis, Humboldt-Universität (2016).

- [15] A. Gulans, S. Kontur, C. Meisenbichler, D. Nabok, P. Pavone, S. Rigamonti, S. Sagmeister, U. Werner and C. Draxl, exciting: a full-potential all-electron package implementing density-functional theory and many-body perturbation theory. *Journal of Physics: Condensed Matter* **26** (36), (2014), 363202.
- [16] Caterina Cocchi and Claudia Draxl, Bound excitons and many-body effects in x-ray absorption spectra of azobenzene-functionalized self-assembled monolayers. *Phys. Rev. B* **92**, (2015), 205105.
- [17] P. Väterlein, M. Schmelzer, J. Taborski, T. Krause, F. Viczian, M. Bäslér, R. Fink, E. Umbach and W. Wurth, Orientation and bonding of thiophene and 2,2'-bithiophene on Ag(111): a combined near edge extended X-ray absorption fine structure and X α scattered-wave study. *Surface Science* **452** (1), (2000), 20 – 32.
- [18] A. P. Hitchcock, J. A. Horsley and J. Stöhr, Inner shell excitation of thiophene and thiolane: Gas, solid, and monolayer states. *The Journal of Chemical Physics* **85** (9), (1986), 4835–4848.
- [19] J. Stöhr, J. L. Gland, E. B. Kollin, R. J. Koestner, Allen L. Johnson, E. L. Muetterties and F. Sette, Desulfurization and structural transformation of thiophene on the Pt(111) surface. *Phys. Rev. Lett.* **53**, (1984), 2161–2164.
- [20] C. Grazioli, O. Baseggio, M. Stener, G. Fronzoni, M. de Simone, M. Coreno, A. Guarnaccio, A. Santagata and M. D’Auria, Study of the electronic structure of short chain oligothiophenes. *The Journal of Chemical Physics* **146** (5), (2017), 054303.
- [21] M. G. Ramsey, F. P. Netzer, D. Steinmüller, D. Steinmüller-Nethl and D. R. Lloyd, Evolution of the core and unoccupied orbitals of biphenyl and bithiophene on Cs doping. *The Journal of Chemical Physics* **97** (6), (1992), 4489–4495.
- [22] G. Koller, R.I.R. Blyth, S.A. Sardar, F.P. Netzer and M.G. Ramsey, Growth of ordered bithiophene layers on the p(2x1)0 reconstructed Cu(110) surface. *Surface Science* **536** (1), (2003), 155 – 165.
- [23] Denis Fichou, ed., Handbook of Oligo- and Polythiophenes. Wiley-VCH Verlag GmbH (2007).
- [24] Markus Schworer and Hans Christoph Wolf, Organic Molecular Solids. Wiley-VCH Verlag GmbH (2008).
- [25] P. A. Chaloner, S. R. Gunatunga and P. B. Hitchcock, Redetermination of 2,2'-bithiophene. *Acta Crystallographica Section C* **50** (12), (1994), 1941–1942.
- [26] Theo Siegrist, Christian Kloc, Robert A. Laudise, Howard E. Katz and Robert C. Haddon, Crystal growth, structure, and electronic band structure of α -4T polymorphs. *Advanced Materials* **10** (5), (1998), 379–382.
- [27] Luciano Antolini, Gilles Horowitz, Fayçal Kouki and Francis Garnier, Polymorphism in oligothiophenes with an even number of thiophene subunits. *Advanced Materials* **10** (5), (1998), 382–385.

- [28] T. Siegrist, R.M. Fleming, R.C. Haddon, R.A. Laudise, A.J. Lovinger, H.E. Katz, P. Bridenbaugh and D.D. Davis, The crystal structure of the high-temperature polymorph of α -hexathienyl (α -6T/HT). *Journal of Materials Research* **10** (9), (1995), 2170–2173.
- [29] B. Servet, G. Horowitz, S. Ries, O. Lagorsse, P. Alnot, A. Yassar, F. Deloffre, P. Srivastava and R. and Hajlaoui, Polymorphism and charge transport in vacuum-evaporated sexithiophene films. *Chemistry of Materials* **6** (10), (1994), 1809–1815.
- [30] Bernhard Klett, Caterina Cocchi, Linus Pithan, Stefan Kowarik and Claudia Draxl, Polymorphism in α -sexithiophene crystals: relative stability and transition path. *Phys. Chem. Chem. Phys.* **18**, (2016), 14603–14609.
- [31] M. Born and R. Oppenheimer, Zur Quantentheorie der Molekeln. *Annalen der Physik* **389** (20), (1927), 457–484.
- [32] P. Hohenberg and W. Kohn, Inhomogeneous electron gas. *Phys. Rev.* **136**, (1964), B864–B871.
- [33] W. Kohn and L. J. Sham, Self-consistent equations including exchange and correlation effects. *Phys. Rev.* **140**, (1965), A1133–A1138.
- [34] John P. Perdew and Yue Wang, Accurate and simple analytic representation of the electron-gas correlation energy. *Phys. Rev. B* **45**, (1992), 13244–13249.
- [35] John P. Perdew, Kieron Burke and Matthias Ernzerhof, Generalized gradient approximation made simple. *Phys. Rev. Lett.* **77**, (1996), 3865–3868.
- [36] Leeor Kronik and Alexandre Tkatchenko, Understanding molecular crystals with dispersion-inclusive density functional theory: Pairwise corrections and beyond. *Accounts of Chemical Research* **47** (11), (2014), 3208–3216, PMID: 24901508.
- [37] Jiří Klimeš and Angelos Michaelides, Perspective: Advances and challenges in treating van der waals dispersion forces in density functional theory. *The Journal of Chemical Physics* **137** (12), (2012), 120901.
- [38] Alexandre Tkatchenko, Lorenz Romaner, Oliver T. Hofmann, Egbert Zojer, Claudia Ambrosch-Draxl and Matthias Scheffler, Van der waals interactions between organic adsorbates and at organic/inorganic interfaces. *MRS Bulletin* **35** (6), (2010), 435–442.
- [39] O. Krogh Andersen, Linear methods in band theory. *Phys. Rev. B* **12**, (1975), 3060–3083.
- [40] S. Cottenier, Density Functional Theory and the family of (L)APW-methods: a step-by-step introduction. ISBN 978-90-807215-1-7 (freely available at http://www.wien2k.at/reg_user/textbooks).
- [41] E. Sjöstedt, L. Nordström and D. J. Singh, An alternative way of linearizing the augmented plane-wave method. *Solid State Communications* **114** (1), (2000), 15 – 20.

- [42] Michael Rohlfing and Steven G. Louie, Electron-hole excitations and optical spectra from first principles. *Phys. Rev. B* **62**, (2000), 4927–4944.
- [43] Giovanni Onida, Lucia Reining and Angel Rubio, Electronic excitations: Density-functional versus many-body green’s-function approaches. *Rev. Mod. Phys.* **74**, (2002), 601–659.
- [44] Peter Puschnig, Excitonic effects in organic semiconductors: An ab-initio study within the lapw method. Dissertation, Karl-Franzens-Universität Graz (2002).
- [45] Stephan Sagmeister, Excitonic effects in solids: Time-dependent density functional theory versus the bethe-salpeter equation. Dissertation, Karl-Franzens-Universität Graz (2009).
- [46] Friedhelm Bechstedt, Many-Body Approach to Electronic Excitations: Concepts and Applications. Springer-Verlag Berlin Heidelberg (2015).
- [47] Lars Hedin, New method for calculating the one-particle Green’s function with application to the electron-gas problem. *Phys. Rev.* **139**, (1965), A796–A823.
- [48] L. J. Sham and T. M. Rice, Many-particle derivation of the effective-mass equation for the wannier exciton. *Phys. Rev.* **144**, (1966), 708–714.
- [49] P. Puschnig, C. Meisenbichler and C. Draxl, Excited State Properties of Organic Semiconductors: Breakdown of the Tamm-Dancoff Approximation. *ArXiv e-prints* .
- [50] D D Koelling and B N Harmon, A technique for relativistic spin-polarised calculations. *Journal of Physics C: Solid State Physics* **10** (16), (1977), 3107.
- [51] Francisco J. Ynduráin, Spin 1/2 particles. In: *Relativistic Quantum Mechanics and Introduction to Field Theory*, 35–66, Springer-Verlag Berlin Heidelberg, Berlin, Heidelberg (1996).
- [52] E. van Lenthe, E. J. Baerends and J. G. Snijders, Relativistic regular two-component hamiltonians. *The Journal of Chemical Physics* **99** (6), (1993), 4597–4610.
- [53] C. S. Schnohr and M. C. Ridgway, eds., *X-Ray Absorption Spectroscopy of Semiconductors*. Springer-Verlag Berlin Heidelberg (2015).
- [54] J. J. Rehr and R. C. Albers, Theoretical approaches to x-ray absorption fine structure. *Rev. Mod. Phys.* **72**, (2000), 621–654.
- [55] G. Bunker, *Introduction to XAFS*. Cambridge University Press (2010).
- [56] P. Yannoulis, R. Dudde, K.H. Frank and E.E. Koch, Orientation of aromatic hydrocarbons on metal surfaces as determined by nexafs. *Surface Science* **189**, (1987), 519 – 528.
- [57] Ulrich Hörmann, Christopher Lorch, Alexander Hinderhofer, Alexander Gerlach, Mark Gruber, Julia Kraus, Benedikt Sykora, Stefan Grob, Theresa Lindlerl, Andreas Wilke, Andreas Opitz, Rickard Hansson, Ana Sofia Anselmo,

- Yusuke Ozawa, Yasuo Nakayama, Hisao Ishii, Norbert Koch, Ellen Moons, Frank Schreiber and Wolfgang Brütting, Voc from a morphology point of view: the influence of molecular orientation on the open circuit voltage of organic planar heterojunction solar cells. *The Journal of Physical Chemistry C* **118** (46), (2014), 26462–26470.
- [58] J. Stöhr and D. A. Outka, Determination of molecular orientations on surfaces from the angular dependence of near-edge x-ray-absorption fine-structure spectra. *Phys. Rev. B* **36**, (1987), 7891–7905.
- [59] S. Berkebile, G. Koller, P. Puschnig, C. Ambrosch-Draxl, F. P. Netzer and M. G. Ramsey, Angle-resolved photoemission of chain-like molecules: the electronic band structure of sexithiophene and sexiphenyl. *Applied Physics A* **95** (1), (2009), 101–105.
- [60] Kerstin Hummer and Claudia Ambrosch-Draxl, Electronic properties of oligoacenes from first principles. *Phys. Rev. B* **72**, (2005), 205205.
- [61] G. Koller, S. Berkebile, M. Oehzelt, P. Puschnig, C. Ambrosch-Draxl, F. P. Netzer and M. G. Ramsey, Intra- and intermolecular band dispersion in an organic crystal. *Science* **317** (5836), (2007), 351–355.
- [62] H. C. Longuet-Higgins, The electronic structure of thiophene and related molecules. *Trans. Faraday Soc.* **45**, (1949), 173–179.
- [63] Michael J. Bielefeld and Donald D. Fitts, Bonding contribution of sulfur d orbitals in thiophene. An extension of the self-consistent field molecular orbital method1. *Journal of the American Chemical Society* **88** (21), (1966), 4804–4810.
- [64] A. S. Davydov, Theory of Molecular Excitons. Springer US (1971).
- [65] Juan Pablo Echeverry and Claudia Draxl, Role of excitonic effects in the absorption spectra of oligothiophene crystals. *In process* .
- [66] Giovanna Fronzoni, Oscar Baseggio, Mauro Stener, Weijie Hua, Guangjun Tian, Yi Luo, Barbara Apicella, Michela Alfè, Monica de Simone, Antti Kivimäki and Marcello Coreno, Vibrationally resolved high-resolution NEXAFS and XPS spectra of phenanthrene and coronene. *The Journal of Chemical Physics* **141** (4), (2014), 044313.
- [67] Markus Schworer and Hans Christoph Wolf, Electronic excited states, excitons, energy transfer. In: Organic Molecular Solids, 125–175, Wiley-VCH Verlag GmbH (2008).
- [68] M. Muccini, M. Schneider, C. Taliani, M. Sokolowski, E. Umbach, D. Beljonne, J. Cornil and J. L. Brédas, Effect of wave-function delocalization on the exciton splitting in organic conjugated materials. *Phys. Rev. B* **62**, (2000), 6296–6300.
- [69] Carlo Taliani and Wolfram Gebauer, Electronic excited states of conjugated oligothiophenes. In: Denis Fichou, ed., Handbook of Oligo- and Polythiophenes, 361–404, Wiley-VCH Verlag GmbH (2007).

- [70] Kerstin Hummer and Claudia Ambrosch-Draxl, Oligoacene exciton binding energies: Their dependence on molecular size. *Phys. Rev. B* **71**, (2005), 081202.
- [71] J. Gierschner, J. Cornil and H.-J. Egelhaaf, Optical bandgaps of α -conjugated organic materials at the polymer limit: Experiment and theory. *Advanced Materials* **19** (2), (2007), 173–191.
- [72] Rupert C. C. Perera and Robert E. LaVilla, Molecular x-ray spectra: S-K β emission and K absorption spectra of thiophene. *The Journal of Chemical Physics* **84** (8), (1986), 4228–4234.
- [73] A. Mijovilovich, L. G. M. Pettersson, S. Mangold, M. Janousch, J. Susini, M. Salome, F. M. F. de Groot and B. M. Weckhuysen, The interpretation of sulfur K-edge XANES spectra: A case study on thiophenic and aliphatic sulfur compounds. *The Journal of Physical Chemistry A* **113** (12), (2009), 2750–2756.
- [74] Graham N. George, Mark J. Hackett, Michael Sansone, Martin L. Gorbaty, Simon R. Kelemen, Roger C. Prince, Hugh H. Harris and Ingrid J. Pickering, Long-range chemical sensitivity in the sulfur K-edge x-ray absorption spectra of substituted thiophenes. *The Journal of Physical Chemistry A* **118** (36), (2014), 7796–7802, pMID: 25116792.
- [75] Shirin Behyan, Yongfeng Hu and Stephen G. Urquhart, Sulfur 1s near edge x-ray absorption fine structure spectroscopy of thiophenic and aromatic thioether compounds. *The Journal of Chemical Physics* **138** (21), (2013), 214302.
- [76] Imanishi Akihito, Yokoyama Toshihiko, Kitajima Yoshinori and Ohta Toshiaki, Structural and electronic properties of adsorbed thiophene on Cu(111) studied by S K-edge x-ray absorption spectroscopy. *Bulletin of the Chemical Society of Japan* **71** (4), (1998), 831–835.
- [77] A. S. Johnson, L. Miseikis, D. A. Wood, D. R. Austin, C. Brahms, S. Jarosch, C. S. Strüber, P. Ye and J. P. Marangos, Measurement of sulfur L_{2,3} and carbon K edge XANES in a polythiophene film using a high harmonic supercontinuum. *Structural Dynamics* **3** (6), (2016), 062603.
- [78] U Gelius, C J Allan, G Johansson, H Siegbahn, D A Allison and K Siegbahn, The ESCA spectra of benzene and the iso-electronic series, thiophene, pyrrole and furan. *Physica Scripta* **3** (5), (1971), 237.
- [79] G. Maccagnani, A. Mangini and S. Pignataro, ESCA study of heterocyclic compounds: Pentatomic saturated derivatives. *Tetrahedron Letters* **13** (36), (1972), 3853 – 3856.
- [80] F. M. F. de Groot, J. C. Fuggle, B. T. Thole and G. A. Sawatzky, $L_{2,3}$ x-ray-absorption edges of d^0 compounds: K^+ , Ca^{2+} , Sc^{3+} , and Ti^{4+} in octahedral symmetry. *Phys. Rev. B* **41**, (1990), 928–937.
- [81] Kerstin Hummer, On the Electro-optical Properties of Oligo-acenes: An An-Initio Study. Shaker Verlag (2003).

A Transformation from Cartesian to Crystalline Axes

As a result of the monoclinic symmetry, the Cartesian axes y and z are equivalent to the crystalline b and c axes. This results in ϵ_{yy} and ϵ_{zz} being equal to ϵ_{bb} and ϵ_{cc} , respectively. The latter defines the response polarized parallel to the long molecular axis, see also Fig. 2.2. It is important to note that the crystalline a axis differs from the Cartesian x axis by the monoclinic angle β . The transformation is given by [81]:

$$\text{Im } \epsilon_{aa} = \begin{pmatrix} \sin \beta & 0 & \cos \beta \end{pmatrix} \cdot \begin{pmatrix} \text{Im } \epsilon_{xx} & 0 & \text{Im } \epsilon_{xz} \\ 0 & \text{Im } \epsilon_{yy} & 0 \\ \text{Im } \epsilon_{xz} & 0 & \text{Im } \epsilon_{zz} \end{pmatrix} \cdot \begin{pmatrix} \sin \beta \\ 0 \\ \cos \beta \end{pmatrix}.$$

For the C K and S $L_{2,3}$ absorption edges, this results in small changes of intensity. In those cases, the Cartesian axes are a good approximation for the crystalline axes. For the S K edge, however, this is not the case. The intensity of the two strongest peaks is significantly redistributed because they contain relevant fractions from the zz and xz components. This is depicted in Fig. A.3 and A.4 for the spectrum from S₁. We want to emphasize that a comparison with experiments on crystalline samples is allowed if the Cartesian components of $\text{Im } \epsilon_{\text{M}}$ are transformed into those corresponding to the crystalline axes.

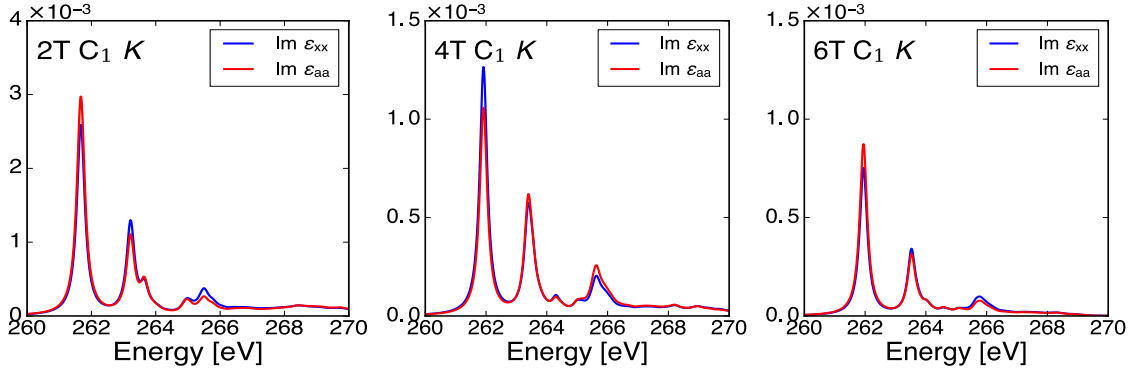


Figure A.1: The Cartesian diagonal x element and its transformation into the crystalline component a for the C₁ K absorption edge of 2T (left), 4T (middle), 6T (right).

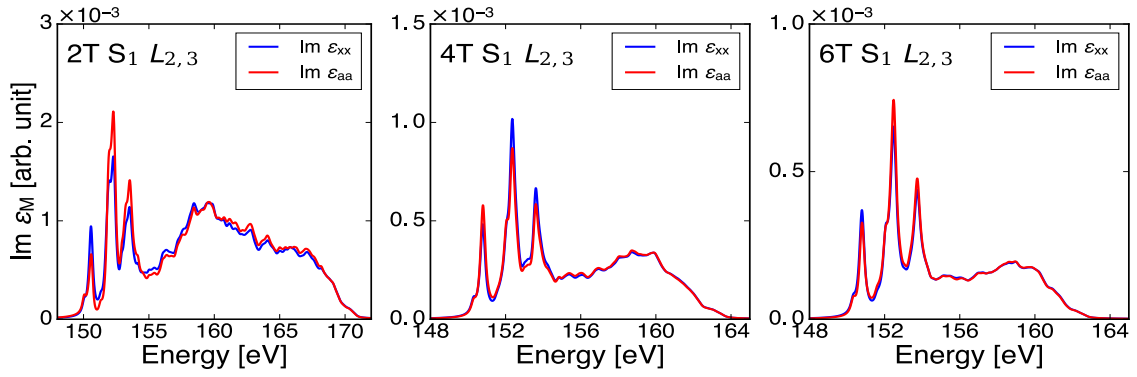


Figure A.2: The Cartesian diagonal x element and its transformation into the crystalline component a for the $S_1 L_{2,3}$ absorption edge of 2T (left), 4T (middle), 6T (right).

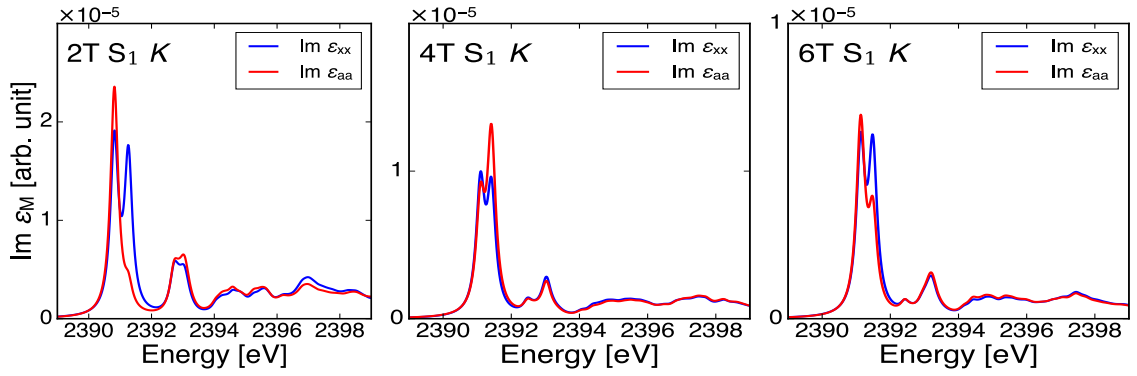


Figure A.3: The Cartesian diagonal x element and its transformation into the crystalline component a for the $S_1 K$ absorption edge of 2T (left), 4T (middle), 6T (right).

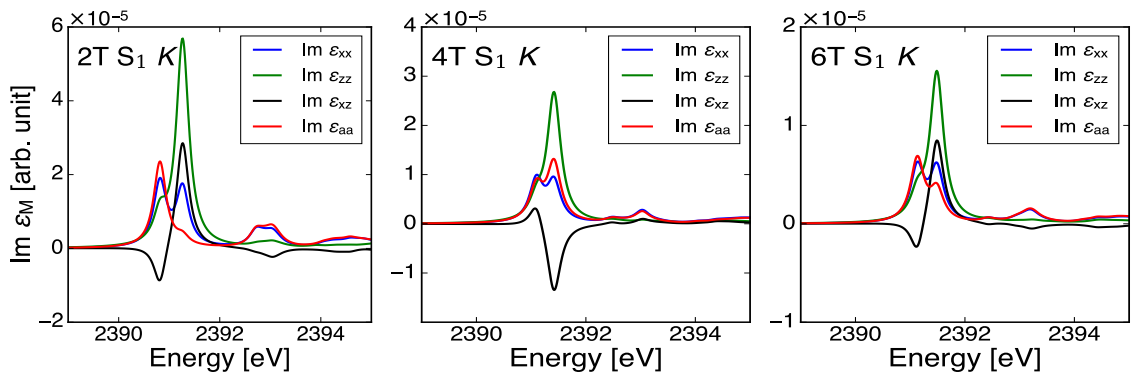


Figure A.4: Redistribution of intensity for the two lowest peaks results in the crystalline aa component for the $S_1 K$ absorption edge of 2T (left), 4T (middle), 6T (right).

B Supplement to Chapter VI

Visualization of LUMO subbands

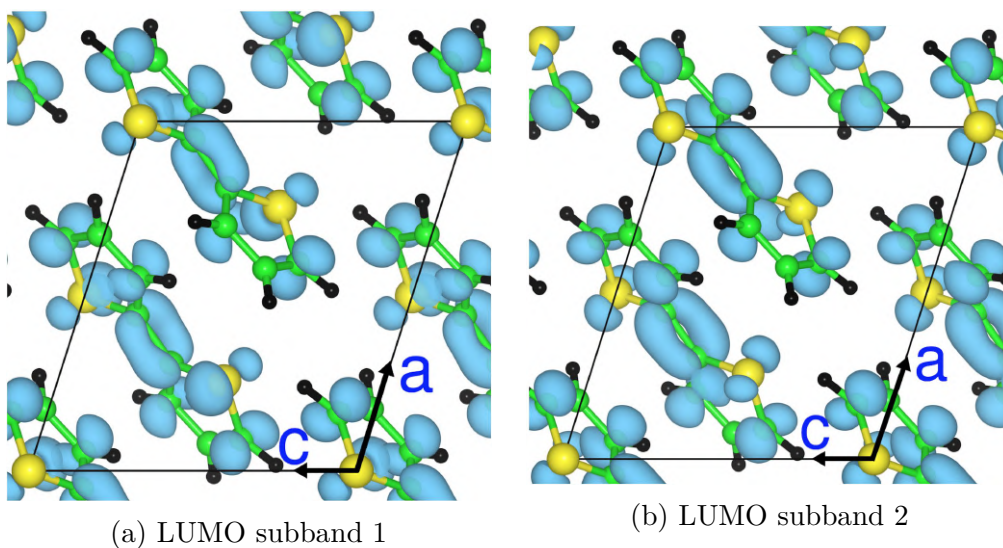


Figure B.1: Lowest unoccupied molecular orbitals of the 2T crystal. An isovalue of 0.002 is used for the isosurfaces. The unit cell is indicated by the rectangle.

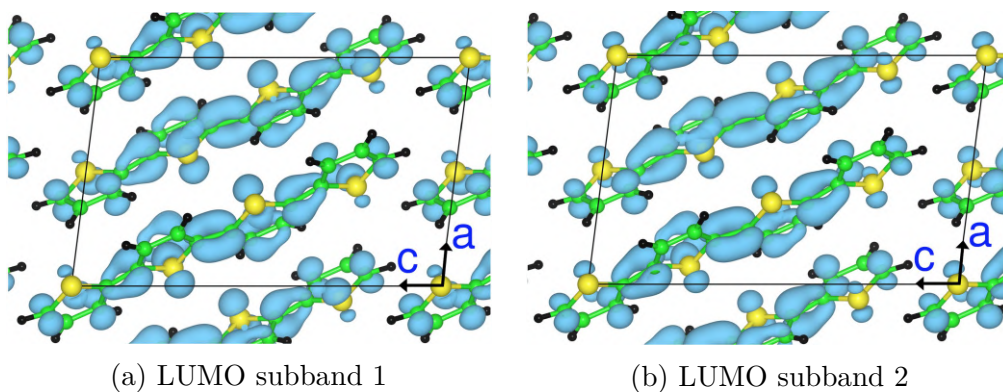


Figure B.2: Lowest unoccupied molecular orbitals of the 4T crystal. An isovalue of 0.001 is used for the isosurfaces. The unit cell is indicated by the rectangle.

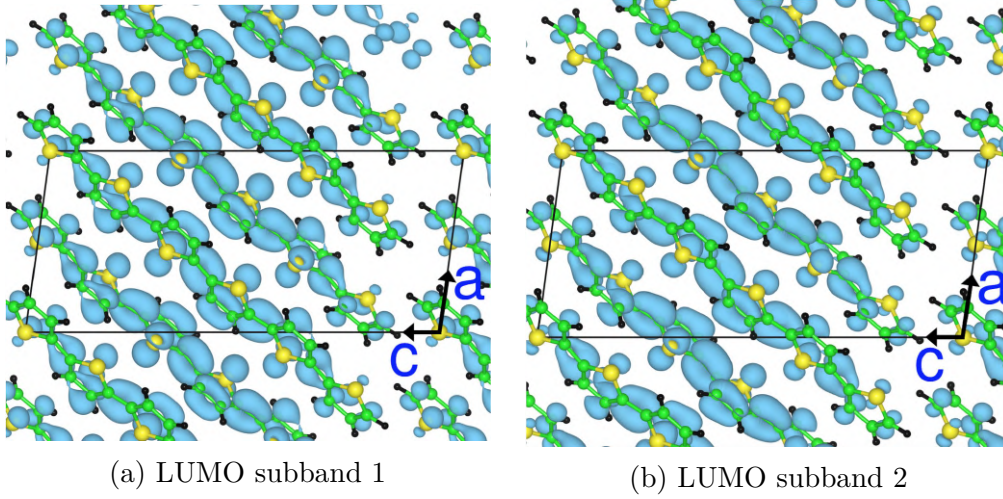


Figure B.3: Lowest unoccupied molecular orbitals of the 6T crystal. An isovalue of 0.0005 is used for the isosurfaces. The unit cell is indicated by the rectangle.

C K absorption edge

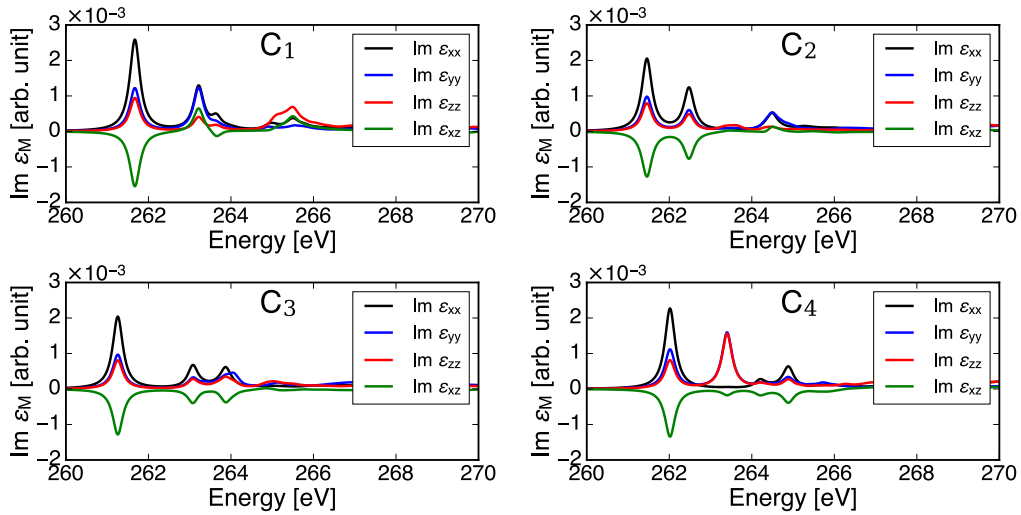


Figure B.4: Non-vanishing components of the imaginary part of the macroscopic dielectric tensor of the four inequivalent C K absorption edges of 2T. Shown is the solution of the full BSE.

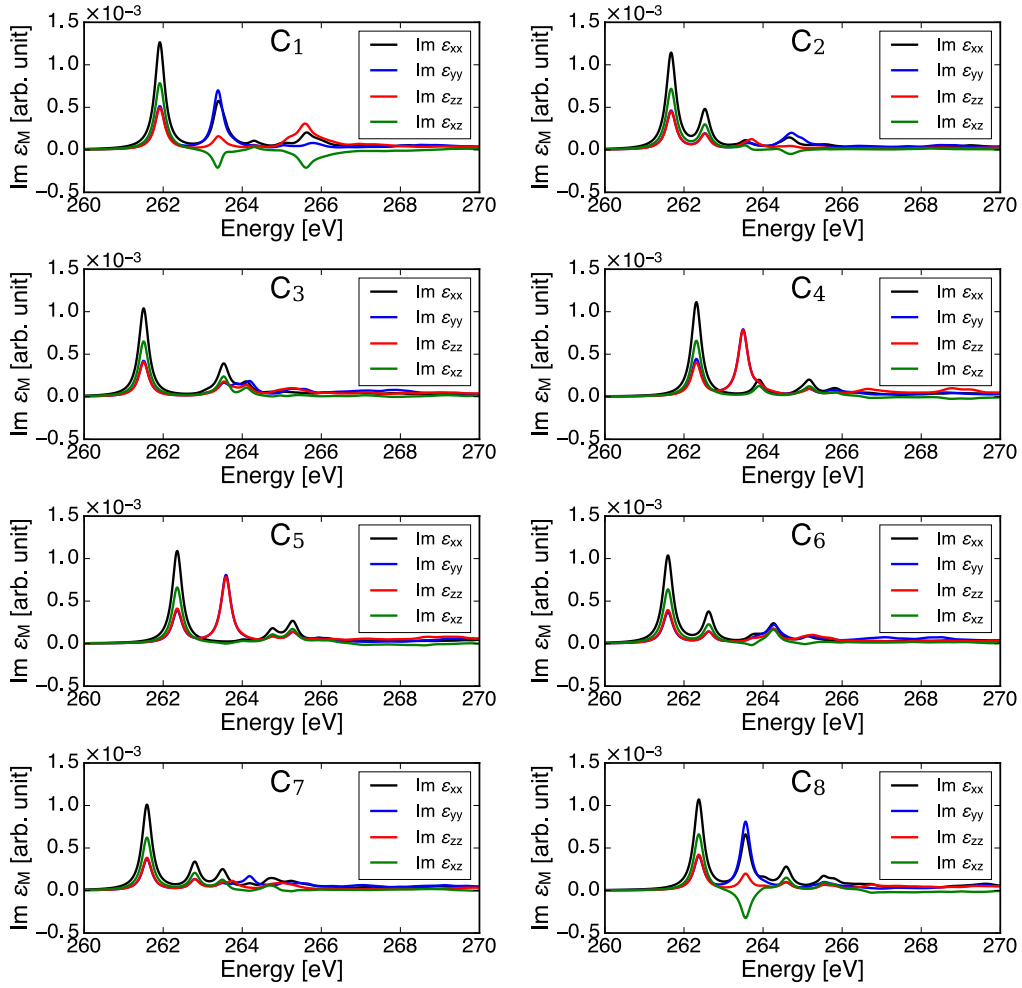


Figure B.5: Non-vanishing components of the imaginary part of the macroscopic dielectric tensor of the eight inequivalent $C K$ absorption edges of 4T. Shown is the solution of the full BSE.

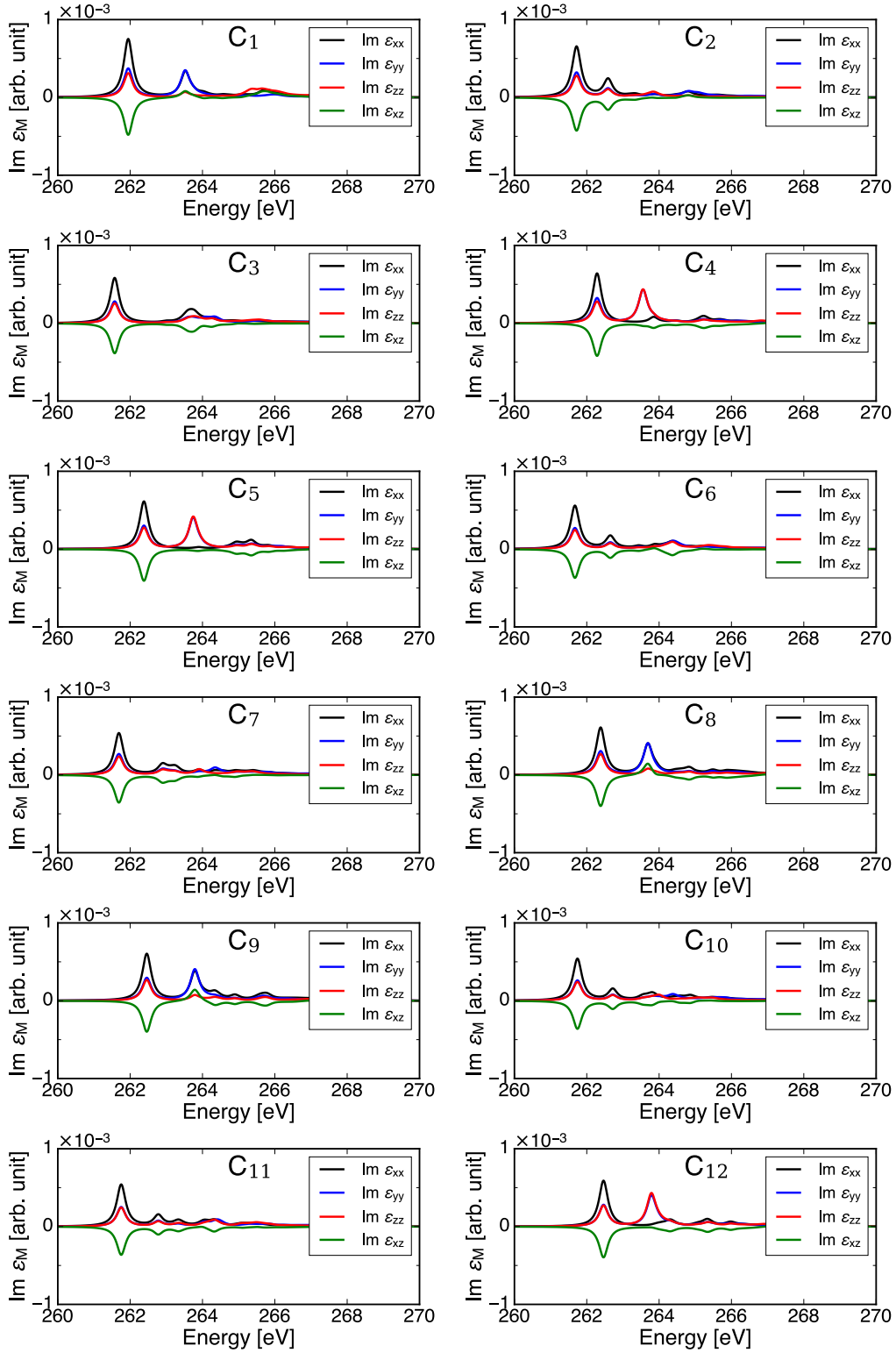


Figure B.6: Non-vanishing components of the imaginary part of the macroscopic dielectric tensor of the twelve inequivalent C K absorption edges of 6T. Shown is the solution of the full BSE.

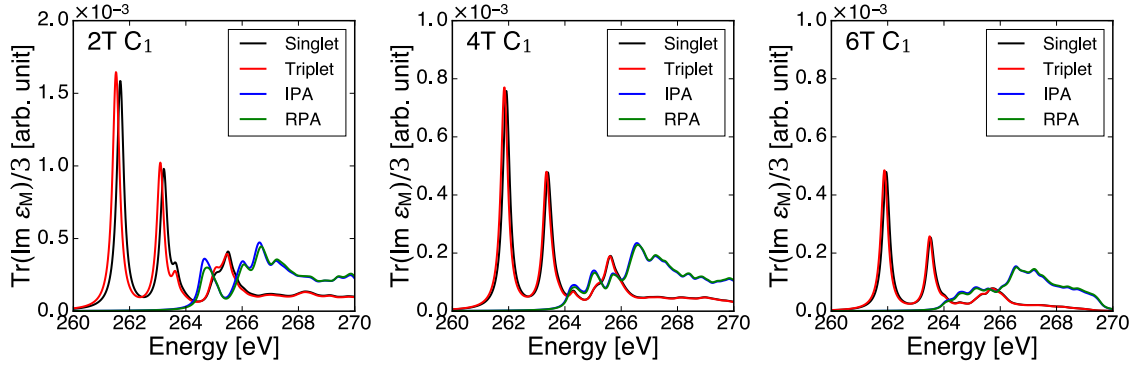


Figure B.7: Influences of the different contributions to the BSE Hamiltonian on the C_1 K absorption edge of 2T (left), 4T (middle), 6T (right). Shown is the solution of the full BSE in black, the independent particle approximation (IPA) in blue, the triplet solution with $H^x = 0$ in red, and the random phase approximation with $H^c = 0$ in green.

S K absorption edge

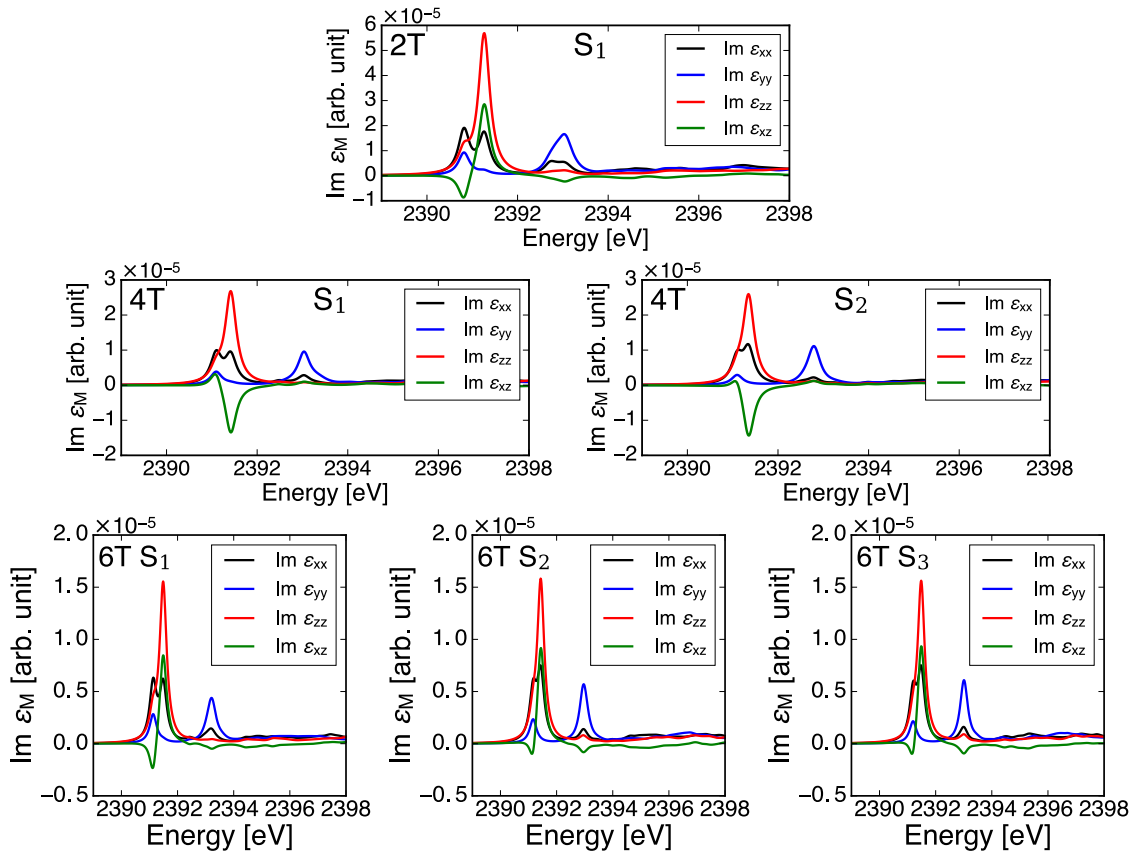


Figure B.8: Non-vanishing components of the imaginary part of the macroscopic dielectric tensor of the inequivalent S K absorption edges of 2T (top), 4T (middle), and 6T (bottom). Shown is the solution of the full BSE.

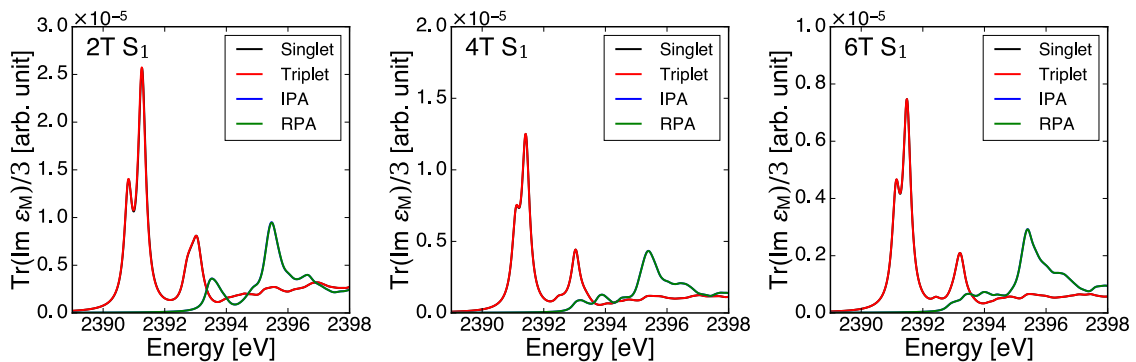


Figure B.9: Influences of the different contributions to the BSE Hamiltonian on the S_1 K absorption edge of 2T (left), 4T (middle), 6T (right). Shown is the solution of the full BSE in black, the independent particle approximation (IPA) in blue, the triplet solution with $H^x = 0$ in red, and the random phase approximation with $H^c = 0$ in green.

S $L_{2,3}$ absorption edge

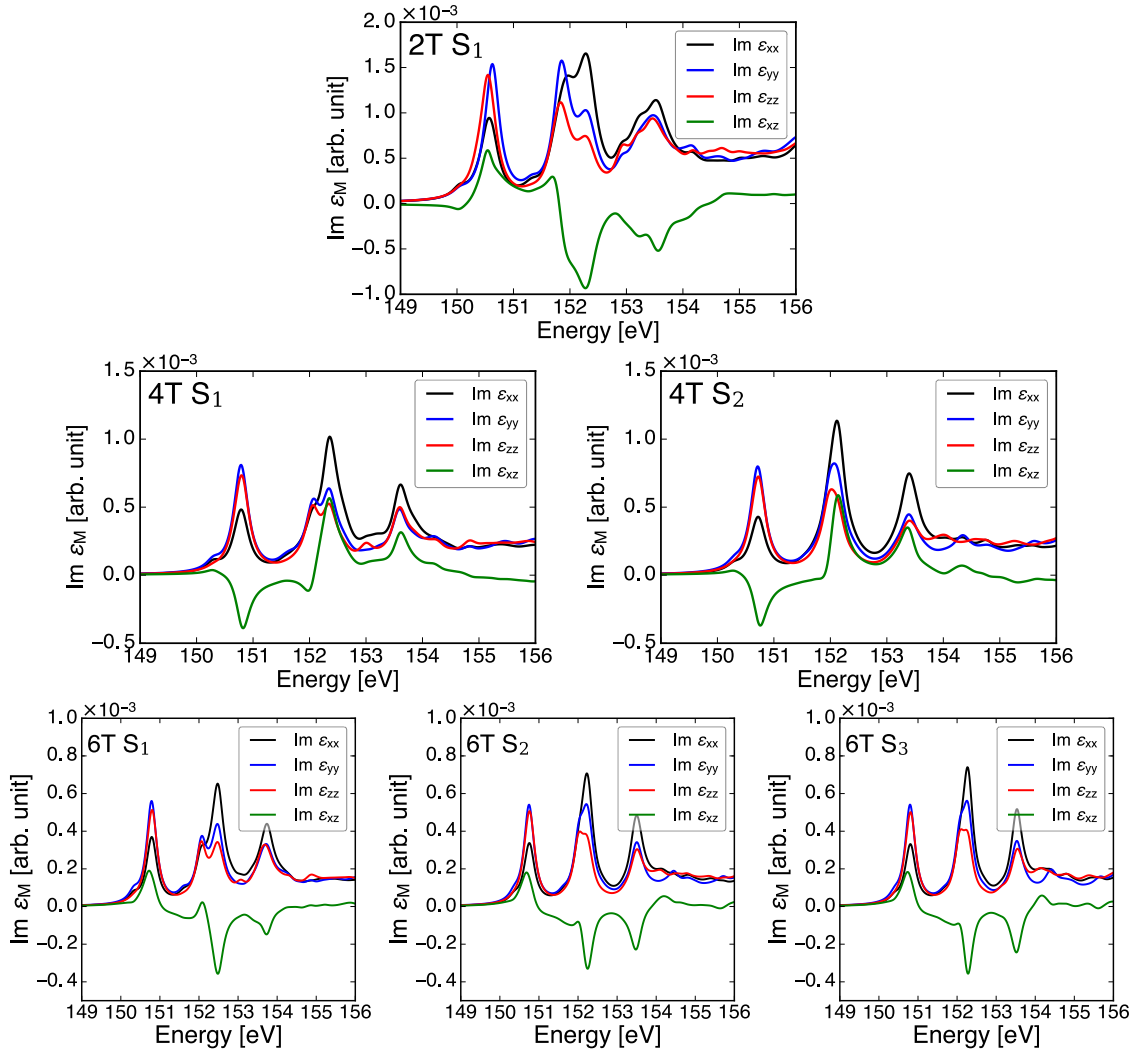


Figure B.10: Non-vanishing components of the imaginary part of the macroscopic dielectric tensor of the inequivalent S $L_{2,3}$ absorption edges of 2T (top), 4T (middle), and 6T (bottom). Shown is the solution of the full BSE.

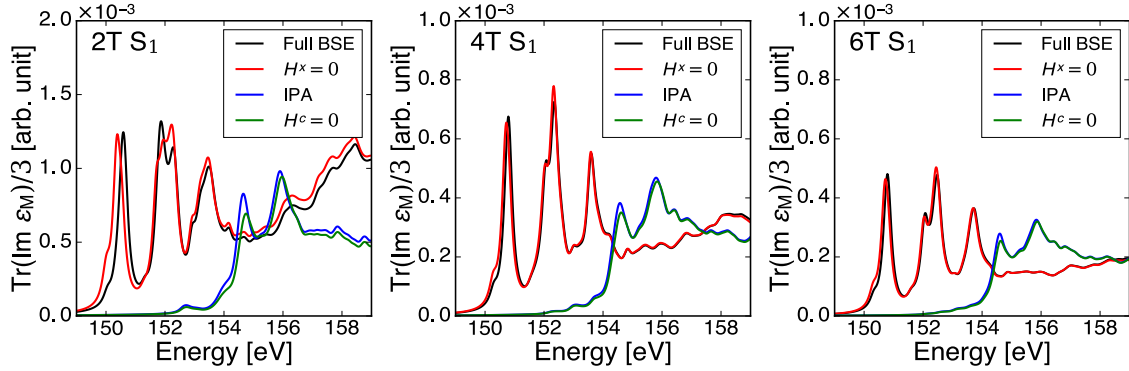


Figure B.11: Influences of the different contributions to the BSE Hamiltonian on the S_1 $L_{2,3}$ absorption edge of 2T (left), 4T (middle), 6T (right). Shown is the solution of the full BSE in black, the independent particle approximation (IPA) in blue, the BSE with $H^x = 0$ in red, and the random phase approximation with $H^c = 0$ in green.

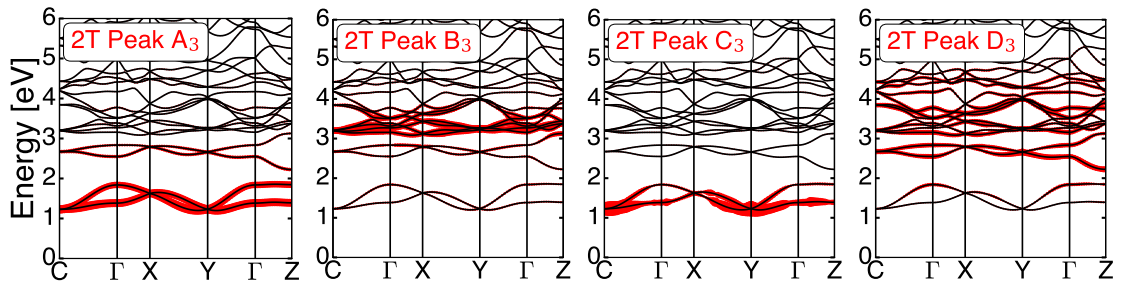


Figure B.12: Excitonic weights of the intense peaks of the S $L_{2,3}$ absorption edge in crystalline 2T plotted on top of the Kohn-Sham band structure. The size of the red circles represents their magnitude.

Selbstständigkeitserklärung

Hiermit versichere ich, Konstantin Lion, dass ich meine Abschlussarbeit selbstständig verfasst und keine anderen als die angegebenen Quellen und Hilfsmittel benutzt habe.

.....
(Datum und Unterschrift)